



Diurnal aging of biomass burning emissions: Impacts on secondary organic aerosol formation and oxidative potential

Maria P. Georgopoulou^{1,2}, Kalliopi Florou¹, Angeliki Matrali^{1,2}, Georgia Starida², Christos Kaltsonoudis¹, Athanasios Nenes^{1,3,*}, and Spyros N. Pandis^{1,2,*}

¹Institute of Chemical Engineering Sciences, Foundation for Research and Technology Hellas (FORTH/ICE-HT), Patras 26504, Greece

²Department of Chemical Engineering, University of Patras, Patras 26504, Greece

³Laboratory of Atmospheric Processes and their Impacts, School of Architecture, Civil & Environmental Engineering École Polytechnique Fédérale de Lausanne CH-1015 Lausanne, Switzerland

*Correspondence to: Spyros Pandis (spyros@chemeng.upatras.gr) and Athanasios Nenes (athanasios.nenes@epfl.ch)

1 Abstract

2 Residential biomass burning is an important wintertime source of aerosols. These particles are
3 subjected to complex diurnal aging processes in the atmosphere, contributing to urban and
4 regional air pollution. The cumulative impact of these aging cycles on aerosol composition and
5 oxidative potential, a key toxicity metric, remains unclear. This study examined the oxidation
6 cycles of biomass burning emissions during day-to-night and night-to-day transitions in the
7 FORTH (Foundation for Research and Technology – Hellas) atmospheric simulation chamber,
8 focusing on emissions from burning of olive wood. The final high-resolution AMS spectra of
9 biomass burning organic aerosol (bbOA) after either oxidation cycle were almost identical (R^2
10 > 0.99 , $\theta = 3^\circ$). This indicates transformation into similar biomass burning secondary organic
11 aerosol (bbSOA) regardless of the initial step of the diurnal cycle. A 56% average increase in
12 the bbOA oxygen-to-carbon (O:C) ratio was observed during both cycle cases (from $0.38 \pm$
13 0.06 for the fresh to 0.59 ± 0.07 after aging). Additional OA mass was produced after the two
14 cycles, varying from 35 to 90 % of the initial OA. The aging of the emissions led to a final
15 water-soluble oxidative potential (WS-OP) increase of 60% to $68 \pm 18 \text{ pmol min}^{-1} \mu\text{g}^{-1}$ for both
16 cycles, but with notably different transient values that depend on the order of the oxidation
17 regimes. The effect of each oxidation regime on the WS-OP of the bbOA depends on the
18 air mass history. The evolution of the WS-OP was not well correlated with that of the O:C.



19 **1 Introduction**

20 Biomass burning for residential heating has significantly increased over the past two decades
21 in several countries, primarily driven by rising energy costs and efforts to reduce the use of
22 fossil fuels (Alper et al., 2020). Alongside contributions from wildfires, residential biomass
23 burning has emerged as a major source of urban and regional pollution worldwide (Zauqi-
24 Sajani et al., 2024). Solid biomass currently represents nearly 45% of the total bioenergy supply
25 in the EU, 40% of which is allocated to residential heating, with an anticipated 20% increase
26 projected by 2050 (IEA, 2019, 2021; Reid et al., 2020). This upward trend in the residential
27 burning of solid biomass, particularly wood, has raised serious concerns regarding air quality
28 and human health (Cincinelli et al., 2019; Guercio et al., 2021; Pardo et al., 2024).

29 Particles emitted from biomass burning consist of organic compounds, elemental carbon
30 (EC), sulfates, nitrates, ammonium, and ash (Jiang et al., 2024). Biomass burning emissions
31 also include a range of gases; carbon monoxide (Shen et al., 2020), volatile organic compounds
32 (VOCs) such as aldehydes, ketones, and organic acids (Zhang et al., 2021; Huang et al., 2022),
33 carcinogenic polycyclic aromatic hydrocarbons (PAHs and oxy-PAHs) (Tsiodra et al., 2021,
34 2024; Lim et al., 2022), as well as nitrogen oxides and ammonia (Bray et al., 2021). The emitted
35 VOCs contribute to the formation of biomass burning secondary organic aerosol (bbSOA) and
36 can have direct health effects (Fang et al., 2021). The emission profile of these pollutants is
37 variable, influenced by factors such as fuel type and quality (e.g., logs vs. pellets; hardwood
38 vs. softwood; certified vs. non-certified wood, moisture content etc.), burning conditions (e.g.,
39 flaming vs. smoldering, air/oxygen supply, and dilution), and the type of combustion appliance
40 (Fachinger et al., 2017; Nyström et al., 2017; Price-Allison et al., 2021; Trubetskaya et al.,
41 2021).

42 After their release, biomass burning emissions are subject to chemical transformations
43 through homogeneous or heterogeneous reactions, that differ between daytime and nighttime
44 (Donahue et al., 2012; Hodshire et al., 2019; Yazdani et al., 2023). During these reactions, a
45 significant amount of SOA (Yazdani et al., 2023) and reactive oxygen species (ROS) (Wang
46 et al., 2023) can be generated. Hennigan et al. (2011) reported significant variability in bbSOA
47 formation during the photo-oxidation of different emissions. Yazdani et al. (2023) reported that
48 after 6 to 10 hours of daytime exposure, up to 30% (with an average of 15%) of the primary
49 bbOA (bbPOA) mass was oxidized, forming bbSOA that was predominantly composed of
50 acids. The coupled gas-particle partitioning, and reaction of semi-volatile vapors (SVOCs) may
51 play an important role in the processing of bbPOA (Hennigan et al., 2011; Srivastava et al.,



2022). Li et al. (2024) demonstrated that intermediate volatility species (IVOCs) can contribute approximately 70% of the formed bbSOA, more than twice the contribution from VOCs.

The nighttime oxidation of biomass burning emissions by the nitrate radical (NO_3) also leads to rapid aerosol changes (Kodros et al., 2020), but to a lesser extent compared to OH oxidation (Yazdani et al., 2023). In some cases, a doubling of bbOA levels compared to the initial primary bbOA has been observed. This increase has been attributed to gas-phase reactions between the NO_3 radical and mainly phenolic compounds or furanic aldehydes (Hartikainen et al., 2018). Moreover, a substantial increase (7-100%) in the aerosol oxygen-to-carbon (O:C) ratio, as well as in the mass of organic nitrates in bbOA has been reported, as result of nocturnal aging (Kiendler-Scharr et al., 2016; Kodros et al., 2022; Yazdani et al., 2023).

To date, field and atmospheric simulation chamber studies have focused on the oxidation of biomass burning emissions during either daytime or nighttime oxidation regimes, driven respectively by OH and NO_3 radicals (Hennigan et al., 2011; Fry et al., 2014; Hodshire et al., 2019; Jorga et al., 2021; Kodros et al., 2022; Wang et al., 2023; Yazdani et al., 2023). While such investigations have significantly advanced our understanding of the individual effects of these oxidation regimes, they do not fully capture the real-world evolution of biomass burning aerosols, which undergo multiple repeated cycles of daytime and nighttime chemistry during their atmospheric lifetime. Studies on successive aging from daytime and nighttime cycling do exist but have focused on the changes of the optical and chemical properties of bbOA and the gas-particle phase partitioning of semi- and intermediate-volatility organic compounds (Tiitta et al., 2016; Hartikainen et al., 2018; Cappa et al., 2020; Che et al., 2022; Desservettaz et al., 2023; Yazdani et al., 2023). These alternating oxidation regimes cause successive changes in chemical composition, reactivity, and toxicity (Li et al., 2021, 2023; Tomlin et al., 2022; He et al., 2024) that are not well understood. Consequently, the timing of atmospheric BB emissions, being released during the day or night, may also influence the chemical trajectory of BB aerosol aging and therefore affect its composition and properties, including toxicity.

Biomass burning particles are significant sources of reactive oxygen species (ROS), including free radicals (e.g., OH, RO_2 , HO_2) and non-radicals (e.g., $^1\text{O}_2$, H_2O_2). Upon inhalation, these species interact with biological tissues and can disrupt cellular redox balance, triggering (or propagating) oxidative stress and systemic health effects (Costabile et al., 2023). The ability of particulate matter (PM) to catalyze ROS production, known as oxidative potential (OP), is a critical metric linking aerosol exposure to health outcomes (Zhang et al., 2022; Dominutti et al., 2025). Among the various in vivo and in vitro methods developed to



quantify OP (Ng et al., 2019), the abiotic dithiothreitol (DTT) assay is the most well established one, providing a measure of the water-soluble OP (WS-OP) of aerosols through the depletion of surrogate DTT in aerosol extracts (Cho et al., 2005). The broad sensitivity of this method to diverse sources of ROS in aerosols with long lifetimes (Gao et al., 2020; Rao et al., 2020), along with its optimization over the years (Fang et al., 2015; Puthussery et al., 2020) to provide more rapid measurements of water-soluble OP (WS-OP), makes it highly suitable for large-scale studies. Studies using the DTT assay have identified bbOA and SOA as dominant contributors to DTT activity, accounting respectively for 35% and 30% of total OP in ambient aerosols in the Southeastern USA (Verma et al., 2015). More recent studies confirm that biomass burning is a significant source of OP in diverse environments, highlighting the importance of understanding diurnal variations in OP from biomass burning (Paraskevopoulou et al., 2019, 2022; Mylonaki et al., 2024).

Photochemical aging during daytime oxidation promotes particle-bound ROS production, enhancing the OP of the aged aerosols (Li et al., 2021; Wang et al., 2023). For bbOA, the OP was found to increase by a factor of two (2.1 ± 0.9) after multiple days (68 h) of atmospheric aging (Wong et al., 2019). This implies that the health impacts of bbOA may extend far from its sources, as it ages and becomes part of the background aerosol (Vasilakopoulou et al., 2023; Mylonaki et al., 2024).

While it is well-established that bbOA ages rapidly at night, the effects of its nocturnal aging on aerosol OP are poorly understood. Moreover, to our knowledge no studies have yet investigated how the oxidation sequence (day-to-night and night-to-day) affects aerosol chemical composition, aging trajectory, and toxicity (i.e., evolution of OP). This study aims to address these knowledge gaps through controlled chamber experiments simulating realistic diurnal oxidation cycles. In these experiments, fresh biomass burning emissions undergo sequential aging, either through daytime oxidation followed by nighttime oxidation or the reverse. By comparing day-to-night and night-to-day sequences, we aim to elucidate the interplay of oxidation regimes on aerosol chemical evolution and OP, providing novel insights into the health impacts of diurnally aged biomass burning aerosols.

2 Methods

2.1 Atmospheric simulation chamber experiments

Emission aging experiments took place at the FORTH-ASC chamber facility at Patras, Greece. Figure 1 illustrates the setup used for conducting the experiments. Fresh biomass



118 burning emissions were produced in the combustion facility beneath FORTH-ASC by a
119 residential wood stove, fed with commercially available olive wood logs and branches. This
120 type of hardwood is widely used as a fuel in Greece. The emissions were diluted before their
121 injection into the smog chamber, using a custom-made dilution device that was located at the
122 chamber inlet.

123 The FORTH-ASC consists of 10 m³ squared Teflon chamber, located inside a 30 m³
124 reflective room (polished interior aluminium walls), which is temperature-regulated and
125 equipped with ultraviolet lights (Osram, L 36W/73 UV lamps). This setup yields a maximum
126 NO₂ photo-dissociation rate coefficient (J_{NO_2}) of 0.5 min⁻¹ when all lights are on. In this study
127 1/3 to 2/3 of the ultraviolet lights were used during photooxidation, resulting in a NO₂ photo-
128 dissociation rate coefficient (J_{NO_2}) of 0.17 to 0.33 min⁻¹.

129 Eight day-to-night (denoted as daytime-first or DN) and eight night-to-day (denoted as
130 nighttime-first or ND) aging experiments were performed under dry (12-24% RH) conditions.
131 Table 1 summarizes the initial aerosol composition and experimental conditions for all the
132 conducted experiments. To investigate the impact of fire starter on biomass burning emissions
133 characteristics, pine kindling mixed with olive logs was used in two of the nighttime-first
134 experiments (ND7, ND8). Pine, which is a softwood, has chemically distinct characteristics
135 compared to olive wood (hardwood) and is used as a kindling material because it burns quickly
136 due to its high resin content.

137 The smog chamber was first flushed with clean air overnight at a rate of 20 L min⁻¹.
138 Approximately 30 min after the combustion ignition in the wood stove, when flaming
139 conditions had been achieved, a fraction of the fresh emissions was diluted with clean air
140 (dilution ratio ranging from 1:5 to 1:10) and was injected into the chamber, which was pre-
141 filled with clean air and regulated to the desired RH level. This resulted in additional dilution
142 (dilution ratio ~1:30) of the emissions. Two high precision mass flow controllers (Bronkhorst
143 EL-FLOW Prestige FG-201CVP), operating at flow rates ranging from 0 to 20 L min⁻¹, were
144 used; one to supply clean air to the smog chamber during its filling and cleaning stages, and
145 the other to supply clean air to the dilution system. The initial PM₁ concentration achieved in
146 the chamber was 112 ± 56 µg m⁻³ on average (Table 1). The fresh emissions were left to
147 equilibrate and were characterized for about 2 hours. 30-90 ppb of d₉-butanol (98%, Cambridge
148 Isotope Laboratories) was also injected in the chamber as a tracer to determine the
149 concentration of OH radicals (Barnett et al., 2012).



150 Subsequently, in daytime-first experiments, the UV lights were turned on, initiating the
151 daytime aging of fresh biomass burning emissions by OH radicals for at least 2 hours, without
152 the addition of further oxidants. This oxidation step was then followed by at least 2 hours of
153 aging with NO₃ radicals under dark conditions. To initiate NO₃ radical formation, NO₂ and O₃
154 were injected into the chamber at concentrations of 50-150 ppb, and 60-280 ppb, respectively.
155 During nighttime-first cycling experiments, the same oxidation steps were performed but in
156 reverse order. In daytime-first experiments, “time zero” was defined as the moment when the
157 UV lights were turned on, whereas in nighttime-first experiments, it was the point at which O₃
158 was injected.

159 Particle wall losses were also characterized for each experiment. After the completion of
160 the two oxidation stages ammonium sulfate ((NH₄)₂SO₄ ≥99 %, Sigma Aldrich) was injected
161 into the chamber and its loss rate was monitored for at least 3 hours. The dry seeds were
162 produced by atomizing a (NH₄)₂SO₄ solution using a TSI atomizer (model 3076) and drying
163 the resulting droplets with a diffusion silica gel dryer (Fig. 1), as described in Wang et al.
164 (2018).

165 2.2 Online instrumentation

166 A suite of instrumentation was used for the online characterization of both particle and gas-
167 phase pollutants (Fig. 1). A scanning mobility particle sizer (SMPS; Classifier) model 3080;
168 DMA, model 3081, TSI) coupled to a butanol-based condensation particle counter (CPC,
169 model 3775 high, TSI), was used for the measurement of the number and volume size
170 distributions (mobility diameter in the range of 13–700 nm) of the aerosol particles. The SMPS
171 sampled every 3 min with its sheath flow rate set at 3 L min⁻¹ and the sample flow rate at 0.6
172 L min⁻¹. A high-resolution time-of-flight aerosol mass spectrometer (HR-ToF-AMS, Aerodyne
173 Research Inc.), working in V mode with vaporizer temperature set at 600°C and sampling flow
174 rate of approximately 0.1 L min⁻¹, was used for monitoring the time evolution of the non-
175 refractory organic and inorganic PM₁ aerosol composition with time resolution of 3 min.
176 Aerosol absorption and black carbon (BC) concentration were measured with a seven-
177 wavelength aethalometer (Magee Scientific, Model AE33-7), sampling at 2 L min⁻¹. VOCs
178 were measured using a proton transfer reaction mass spectrometer (PTR-QMS 500, Ionicon
179 Analytik), sampling at 0.5 L min⁻¹. The drift tube was maintained at 2.3 mbar and operated at
180 600 V. A detailed explanation of the PTR-MS operational parameters and the calibration
181 procedure using VOC standards can be found in in Kaltsonoudis et al. (2016). Concentrations
182 of carbon monoxide (CO) and dioxide (CO₂), sulfur dioxide (SO₂), ozone (O₃) and nitrogen



183 oxides (NO_x) were measured using the corresponding monitors; CO (Teledyne model 300E),
184 CO_2 (Teledyne model T360), (Thermo model 43i-TLE), O_3 (Teledyne model 400E), NO and
185 NO_2 (Teledyne model T201). The total sampling flow rate of all monitors was 3.8 L min^{-1} .

186 2.3 Online data analysis methodology

187 The initial combustion conditions in the chamber were characterized by calculating the
188 modified combustion efficiency (MCE) as the ratio of the carbon dioxide (CO_2) to the sum of
189 CO_2 and carbon monoxide (CO) (Yokelson et al., 1996).

190 The HR-ToF-AMS data were analyzed using the packages SQUIRREL (Sequential Igor
191 data Retrieval; v1.57) and PIKA (Peak Integration by Key Analysis; v1.16) incorporated in
192 Igor Pro software (WaveMetrics; version 6.37). The method described in Canagaratna et al.
193 (2015) was used to estimate of elemental O:C ratio. The AMS collection efficiency (CE) and
194 the corresponding OA density have been determined using the algorithm proposed by
195 Kostenidou et al. (2007). This approach combines the volume distributions obtained from the
196 SMPS and the mass distributions of the main PM_{10} components from the AMS. The BC
197 concentration obtained by the aethalometer was also included in the calculation, assuming a
198 size distribution for BC similar to that of OA.

199 SMPS measurements were corrected using size-dependent wall loss rate constants,
200 estimated by monitoring the decline in the mass concentration of $(\text{NH}_4)_2\text{SO}_4$ particles injected
201 into the chamber at the end of each experiment. Practically size independent first-order wall
202 loss rates were observed for particle diameters ranging from 60 to 700 nm. Based on this, the
203 concentrations of the non-refractory PM_{10} aerosol species measured by the AMS were corrected
204 using one experiment-specific, size-independent wall loss rate constant that was 0.15 ± 0.05
205 h^{-1} on average.

206 The total OA was split into primary (bbPOA) and secondary (bbSOA) following the
207 approach proposed by Jorga et al. (2020) and applied for bbOA by Kodros et al. (2022). To
208 quantify the variation between primary and secondary bbOA mass spectra, obtained by the
209 AMS, the theta angle (θ) was estimated (Kostenidou et al., 2009). This angle represents the
210 inner product of the two spectra (i.e., fresh and aged one), considered as n-dimensional vectors
211 (n is to the number of the mass-to-charge (m/z) ratios). Theta angles less than 10° imply high
212 similarity, while major differences between two compared spectra correspond to θ values
213 higher than 25° (Florou et al., 2023). The approach described in Kiendler-Scharr et al. (2016)
214 was used to quantify the particulate organic nitrate (ON). In the present study the minimum



215 measured $\text{NO}_2^+/\text{NO}^+$ ratio in all experiments was 0.04. The corresponding measured ratio for
216 pure NH_4NO_3 , determined through calibration, was equal to 0.56.

217 Prior to each experiment, background VOC levels in the chamber were measured using
218 the PTR-MS for at least 1 hour. The PTR-MS was unavailable during experiments DN2–DN7.
219 The PTR-MS measurements of the protonated VOCs were background-corrected and averaged
220 at the end (over the last 1 h) of the fresh emissions' stabilization period, as well as at the end
221 (over the last 1 h) of each oxidation step. The final values are summarized in Table S1 of the
222 supplement, along with a classification of the identified VOCs by chemical structure and
223 functional groups.

224 Following the work of Barmet et al. (2012), the average OH radical concentration was
225 estimated from the decline/reduction in the concentration of the m/z 66 (protonated mass of d_9 -
226 butanol). A d_9 -butanol reaction rate coefficient equal to $3.4 \times 10^{-12} \text{ cm}^3 \text{ molecule}^{-1} \text{ s}^{-1}$ (at 295
227 K) was assumed (Allani et al., 2021).

228 **2.4 Collection of samples for offline analysis**

229 To investigate the WS-OP of both fresh and aged BB aerosol, as well as to measure their
230 organic (OC) and elemental carbon (EC) content, filter samples (Whatman Tissuquartz
231 2500QAO-UP, 47 mm, 0.45 pore size) were collected for 1 h at the end of the emissions'
232 equilibration period as well as at the end of each oxidation step. Prior to each experiment, blank
233 filter samples were also collected. Sampling was conducted using a filter holder coupled with
234 a $\text{PM}_{2.5}$ cyclone positioned at the chamber exit. An external vacuum pump (Becker VT 4.10,
235 150 Mbar), operating at a flow rate of 16.7 L min^{-1} , was used, with its exhaust connected to a
236 HEPA filter (Whatman 6702-9500). Prior to sampling, the quartz filters were baked at 500°C
237 for 10 h and left in the oven overnight, to remove any absorbed organic material. Each filter
238 was wrapped in prebaked aluminum foil and was kept before and after sampling in sterile
239 polystyrene petri dishes (50 mm, Pall Laboratory). After sampling all filters were stored at a
240 temperature of -20°C , until WS-OP and OC/EC analysis.

241 Tenax sorbent tubes (stainless steel $3.5 \times 1/4$ in tubes, filled with Tenax TA, Markes
242 International) were used to collect VOC samples at specific time intervals. The custom-made
243 sampling system used included a mass flow controller (Alicat Scientific MC-500SCCM-
244 D/5M), the sampling tube, and a diaphragm vacuum pump (AIRPO, Model D2028B 12VDC),
245 operating at a flow of 0.3 L min^{-1} for 1 to 1.5 h, resulting in total collected sample volumes
246 ranging from 18–27 L. After sampling all sorbent tubes were capped with long-term storage



247 brass caps containing PTFE ferrules and were stored in a freezer at -18 °C (Harshman et al.,
248 2016).

249 **2.5 TD-GCMS measurements**

250 The offline determination of VOCs/IVOCs involved a two-step desorption process. The
251 compounds adsorbed in the Tenax tubes were first desorbed using a thermal desorber (UNITY–
252 Air Server-xr, Markes International Ltd.). During thermal desorption (TD), the sorbent tube
253 underwent heating up to 280 °C for 10 min to release all its contents. Subsequently, the
254 desorbed VOCs were captured using Helium (as the carrier gas) and then deposited onto a
255 sorption cold trap at 20 °C. Subsequently, the temperature of the cold trap was gradually
256 increased from 20 °C to 300 °C at a rate of 100 °C s⁻¹, where it remained for 6 min. The retained
257 analytes were then injected into a single quadrupole gas chromatograph-mass spectrometer
258 (GSMS, Shimadzu model QP2010, with helium as carrier gas). The GC-MS system was
259 equipped with an inert capillary column (MEGA-5MS, 30 m length, 0.25 mm inner diameter,
260 0.25 µm film thickness). The oven temperature of the GC column remained at 32°C for
261 approximately 5 min, increasing to 320 °C at 5 °C min⁻¹. MS data acquisition was conducted
262 in full scan mode, scanning within the *m/z* range of 35 to 300 amu. After the analysis, both the
263 Tenax tubes and the GC column were cleaned. Calibration of the system was performed using
264 standards of specific VOCs (EPA labelled) loaded in clean tubes. The species detected by TD-
265 GCMS for a typical experiment (DN4) are presented in Table S2.

266 **2.6 Oxidative potential (OP) measurements**

267 The water-soluble oxidative potential (WS-OP) of redox-active aerosol components was
268 measured using a DTT assay system (Fig. S1) at FORTH/ICE-HT in Patras, Greece, which is
269 based on the semi-automated method of Fang et al. (2015). A detailed description of the system
270 components, operation, measurement protocol, and data treatment, is provided in the
271 Supplementary Information Section S1. Briefly, the fresh and aged aerosol samples (1.5 cm²
272 punches of the collected quartz filters) are extracted, filtered, and incubated with DTT, in
273 excess, under controlled conditions. The DTT is gradually oxidized by ROS in the sample, with
274 its consumption rate (DTT activity, in nmol min⁻¹) determined spectrophotometrically by
275 measuring the absorbance of 2-nitrobenzoic acid (TNB), the derivatization product of DTT
276 with DTNB reagent, at 412 nm at specific time intervals. The WS-OP was calculated by
277 correcting for blank samples and was normalized to the OC mass of the sample, yielding net
278 DTT consumption rates (mass-normalized DTT activity – DTT_m) in pmol min⁻¹µg⁻¹ (Table S3).



OC was quantified via thermal-optical analysis (NIOSH-870 protocol), with an estimated relative standard deviation of $15 \pm 5\%$ for replicate measurements.

3 Results and Discussion

3.1 Characterization of fresh olive wood emissions

Flaming conditions predominated in all experiments, as indicated by the estimated modified combustion efficiency (MCE) that ranged from 0.91 to 0.99 (Table 1) (Li et al., 2015; Briggs et al., 2016). The initial PM_{10} concentration of the fresh olive wood burning emissions in the chamber varied from 47 to $177 \mu\text{g m}^{-3}$ (considering experiments DN1-DN8 and ND1-ND6). This range of concentrations is representative of light to severe biomass burning pollution episodes in polluted urban areas during wintertime (Chen et al., 2022; Luo et al., 2022; Othman et al., 2022). The average AMS collection efficiency (CE) of the fresh emissions averaged 0.8 ± 0.2 , while the mean OA density, calculated following the approach of Kostenidou et al. (2007), was $1.11 \pm 0.12 \text{ g cm}^{-3}$. Estimating the OA density from measured O:C and hydrogen-to-carbon (H:C) ratios, following the Kuwata et al. (2012) approach, yielded an average of $1.18 \pm 0.03 \text{ g cm}^{-3}$.

The fresh aerosol primarily consisted of organics ($95 \pm 3\%$) with OA concentrations ranging from 46 up to $174 \mu\text{g m}^{-3}$ (Table 1). The rest of the aerosol consisted of BC ($2.4 \pm 2.4\%$), nitrates ($1.4 \pm 0.7\%$), sulfates ($0.7 \pm 0.4\%$), chloride ($0.4 \pm 0.2\%$) and ammonium ($0.2 \pm 0.1\%$). In experiment DN3, ammonium sulfate seeds were also present explaining the higher initial sulfate (28%) and ammonium (10%) content.

The initial mass ratio of the organic aerosol to black carbon (OA/BC) ranged from 13 to 263. The OA/BC differs significantly depending on the combustion conditions. When MCE values exceed 0.9, the OA/BC ratio can range between 0.3 to 10^5 (McClure et al., 2020), with higher values indicating more efficient combustion (Novakov et al., 2005). Our OA/BC values indicate relatively efficient wood stove operation.

The average initial oxygen to carbon ratio (O:C) of the bbOA in all olive wood burning experiments was 0.39 ± 0.04 . The average initial hydrogen to carbon ratio (H:C) was 1.67 ± 0.04 ranging from 1.62 to 1.76. These values are consistent with previously reported field and smog chamber O:C and H:C observations for fresh biomass burning aerosols (Ng et al., 2010; Sun et al., 2016; Lim et al., 2019; Kodros et al., 2020; He et al., 2024). The relatively low AMS f_{44}/f_{60} ratios (1.56 ± 0.52) observed in the experiments are representative of fresh biomass



310 burning emissions from wildfires and laboratory wood burning chamber studies (Li et al.,
311 2023).

312 The average high-resolution (HR) fresh bbOA mass spectrum obtained by AMS for the
313 olive wood burning experiments (Fig. S2a) showed predominant fragments at m/z 29 (CHO^+ ,
314 C_2H_5^+), 41 (C_2HO^+ , $\text{C}_2\text{H}_3\text{N}^+$, C_3H_5^+), 43 ($\text{C}_2\text{H}_3\text{O}^+$, C_3H_7^+), 55 ($\text{C}_3\text{H}_3\text{O}^+$, C_4H_7^+), 57 ($\text{C}_3\text{H}_5\text{O}^+$),
315 69 (C_5H_9^+ , $\text{C}_4\text{H}_5\text{O}^+$) and 73 ($\text{C}_3\text{H}_5\text{O}_2^+$), suggesting a significant presence of alkenes, alkanes,
316 and fatty acids. The observed signals at m/z 44 (CO_2^+) and m/z 60 ($\text{C}_2\text{H}_4\text{O}_2^+$), are typical tracer
317 fragments for OOA and bbOA, respectively. The obtained fresh bbOA spectrum profile is quite
318 similar to those reported in previous biomass burning chamber studies that examined wood or
319 pellets burning (He et al., 2010; Kodros et al., 2020, 2022; Florou et al., 2023). The average
320 theta angle θ of the fresh bbOA spectra, calculated for all possible pairs of the olive wood
321 burning experiments in the present study, was on average $9^\circ \pm 7^\circ$ (Fig. S3), indicating a
322 generally similar composition of fresh bbOA.

323 Based on PTR-MS measurements, oxygen-containing compounds contributed the largest
324 portion of the protonated VOCs identified in the fresh emissions (Fig. 2a). Aldehydes,
325 including acetaldehyde (m/z 45; 12.9 ± 3.7 ppb), formaldehyde (m/z 31; 1.6 ± 0.7 ppb), acrolein
326 (m/z 57; 3.5 ± 1.5 ppb), and hexenal (m/z 99; 2.1 ± 1.5 ppb), along with saturated ketones like
327 acetone (m/z 59; 4.7 ± 2.0 ppb) and unsaturated ones such as ethyl vinyl ketone (m/z 85; $2.1 \pm$
328 1.4 ppb), contributed a total of 32.5 ppb, accounting for 19.7% of the measured VOCs.
329 Carboxylic acids, such as formic (m/z 47) and acetic (m/z 61) acids, averaged a total
330 concentration of 8.2 ppb, comprising 5% of the total VOCs (Fig. 2a). The main identified
331 alcohol was 1-butanol (m/z 75), which accounted for 3% of the VOC composition, with
332 concentrations varying from 2.1 ppb to 9.5 ppb across experiments (Table S1). Furans and their
333 derivatives (m/z 69, 83, 113, 147) had an average concentration of 7.9 ppb, accounting for 5%
334 of the total measured VOCs (Fig. 2a).

335 Cyclic and heterocyclic aromatic compounds (with 1-ring or 2-ring structure) contributed
336 approximately 10% to the total VOCs. This includes benzene (m/z 79; 1.5 ± 1.0 ppb) and its
337 substituted forms (m/z 139, 151, 155; 3.3 ppb), toluene (m/z 93; 1.2 ± 0.8 ppb), phenol (m/z 95;
338 2.1 ± 1.7 ppb) and its substituted forms (m/z 121, 135, 149, 169; 2.4 ppb in total), and C8
339 aromatics, including xylenes, (m/z 107; 3.2 ± 2.4 ppb). Other minor contributors, with varying
340 concentrations across experiments, included terpenes and terpenoids (m/z 81 and m/z 137),
341 averaging 2.9 ppb, and naphthalene (m/z 129), averaging 1.4 ± 1.1 ppb. The presence of these
342 aromatic species is corroborated by the Tenax samples, along with compounds like
343 benzonitrile, trimethoxy- benzene, methylindene and benzofurans. For a typical sample of fresh



emissions, chromatographic analysis yielded a variety of phenolic species other than phenol, with functional groups including several alkyl groups (methyl-, dimethyl-,ethyl), but also with oxygenated functional groups (methoxy-, dimethoxy-) as presented in Table S2. Furans comprised approximately 11% of the identifiable VOCs in the offline analysis, with the most prominent being furfural, followed by methyl-furans and methyl- furancarboxaldehyde. In terms of polyaromatic species, similarly to the PTR-QMS observations, the most abundant was naphthalene, while there were several alkyl-substituted naphthalenes present in comparable concentrations. Trace amounts of higher ring number PAHs (e.g., phenanthrene) were also observed. Most of these compounds have been previously reported in biomass burning ambient and laboratory studies (Stockwell et al., 2014; Bruns et al., 2017; Sun et al., 2019; Desservettaz et al., 2023; Florou et al., 2023).

The average WS-OP of the fresh olive wood burning aerosol was 42.9 ± 16.1 pmol $\text{min}^{-1} \mu\text{g}^{-1}$, comparable to toxicity levels reported in literature for the water- and methanol-soluble portion of freshly emitted bbOA, which were also estimated using the acellular DTT assay protocol (Cao et al., 2021; Wang et al., 2023). The WS-OP values ranged from 21.2 ± 5.7 pmol $\text{min}^{-1} \mu\text{g}^{-1}$ (in DN3) to 79 ± 11.3 pmol $\text{min}^{-1} \mu\text{g}^{-1}$ (in DN7) (Table S3).

3.2 Effect of pine kindling on fresh olive wood emissions

In experiments ND7 and ND8, where pine kindling sticks were mixed with olive wood logs, the PM_{10} concentration during the characterization period was $126 \mu\text{g m}^{-3}$ and $276 \mu\text{g m}^{-3}$, respectively (Table 1). High amounts of BC ($67 \mu\text{g m}^{-3}$ and $190 \mu\text{g m}^{-3}$) were produced in these experiments, constituting more than half (53% and 69%) of the total fresh PM_{10} mass. Given the efficient combustion conditions (MCE ranged from 0.96 to 0.98), these elevated BC levels were likely related to the properties of the pine (e.g., higher moisture, ash, and carbon content) compared to the olive logs (Nyström et al., 2017; Trubetskaya et al., 2021). The initial O:C of the fresh bbOA was 0.23 in experiment ND7 and 0.36 in ND8. The O:C in ND7 was the lowest of all experiments.

Comparison of the average fresh bbOA mass spectrum from olive-pine mixed emissions with that of olive logs burning (Fig. S4a) reveals significantly higher peaks at m/z 28 (CO^+ ; +69%), 41 (+36%), 44 (+40%), and 73 (+39%), indicating an increase in certain oxygenated organic species. Additionally, the stronger fractional signals at m/z 91 (C_7H_7^+ ; 104%), and at higher masses, such as m/z 105 (C_8H_9^+ ; 154%), 129 ($\text{C}_{10}\text{H}_9^+$; +166%), suggest a higher relative contribution of cyclic hydrocarbons, PAHs, and other aromatic compounds. The theta angle of the two average fresh spectra was approximately 20° , implying distinct chemical composition



of olive-pine mixed emissions. For the VOCs, while most aromatic compound concentrations were lower in the mixed fuel emissions, their relative contribution to the total VOCs was higher (17.7% vs. 9.6% in olive wood alone), suggesting differences in pyrolysis pathways and thermal degradation mechanisms between the two wood types (Fig. 2a,b). Additionally, monoterpenes (m/z 137 and their fragment m/z 81) showed a significant increase in the mixed emissions, rising from 2.9 ppb to 9.1 ppb, highlighting the influence of pine higher terpene content on VOC composition (Fig. 2). The variations observed in aldehydes, ketones, and heavier PAHs were within the experimental uncertainty. A more detailed breakdown of the absolute and CO₂-normalized VOC concentrations, including experiment-specific observations and comparisons, is provided in the Supplement (Fig. S5, Table S1).

No changes were observed in the WS-OP of the fresh olive-pine mixed emissions compared to fresh olive wood emissions. The corresponding DTT_m values in experiments ND7 and ND8 were 44.7 ± 4.0 pmol min⁻¹ μg⁻¹ and 41.1 ± 3.4 pmol min⁻¹ μg⁻¹, respectively (Table S3). Similar WS-OP values (25 to 45 pmol min⁻¹ μg⁻¹) were reported by Wang et al. (2023) for fresh bbOA from pine combustion under smoldering conditions (MCE=0.61). These values are comparable to the average WS-OP measured in this study for olive wood emissions (42.9 ± 16.1 pmol min⁻¹ μg⁻¹).

3.3 Typical day-to-night (DN) aging experiment

During a typical dry daytime-first oxidation experiment (DN1), two hours before the start of oxidation (at $t = -2$ h), 70 ± 0.4 μg m⁻³ of fresh olive wood burning PM₁ (91 % OA) were injected into the chamber along with approximately 14 ppb of O₃ (Fig. 3). During the emissions equilibration period (-2 to 0 h), the average O:C was 0.43, H:C was 1.67, OA/BC was 17, and the f_{44}/f_{60} ratio was 1.37 (Table 1), and remained quite stable. The WS-OP of the fresh aerosol was estimated at 51.4 ± 4.7 pmol min⁻¹ μg⁻¹ (Table S3).

At time zero ($t = 0$ h), daytime oxidation of the emissions was initiated by turning on the UV lights of the chamber, without adding any oxidants, and allowing the process to proceed for 2 h. Under the given experimental conditions, each hour of UV exposure in the simulation chamber corresponds to approximately 2 hours of atmospheric photochemical oxidation, assuming an average OH concentration of 1.5×10^6 molecule cm⁻³ (Liu et al., 2018; Nault et al., 2018). In DN1, the average OH concentration during this 2-h oxidation period, estimated from the decay of d9-butanol, was 3.2×10^6 molecules cm⁻³, corresponding to an equivalent daytime exposure of 4.3 h. The average O₃ concentration was 33 ± 14 ppb.



409 During this 2-h period the OA (wall loss corrected) increased by $22 \mu\text{g m}^{-3}$ (34%).
410 Organic nitrates also increased by 54% and O_3 reached 56 ppb. The H:C decreased by 4% while
411 the f_{44}/f_{60} more than doubled (3 times higher). The O:C increased from 0.43 to 0.58 (35%),
412 consistent with previous observations (Tiitta et al., 2016). The change in the HR-AMS
413 spectrum of the day-aged OA was modest ($\theta = 8^\circ$). The photochemical processing resulted in
414 an 50% increase of WS-OP ($77.6 \pm 6.3 \text{ pmol min}^{-1} \mu\text{g}^{-1}$) of the bbOA (Table S3). Similar
415 increases of OP have also been reported in previous studies (Wong et al., 2019; Lei et al., 2023;
416 Wang et al., 2023).

417 Furans, terpenes and cyclic aromatic hydrocarbons, major precursors of SOA production,
418 were significantly reduced during daytime (Fig. S6). Aromatic hydrocarbons including toluene
419 (m/z 93), phenol (m/z 95), styrene (m/z 105), C8 aromatics (m/z 107), C9 aromatics (m/z 121),
420 and creosol/2-methoxy-4-methylphenol (m/z 139) reacted and their levels were reduced (Fig.
421 S6b). Daytime aging also led to small changes (1 ppb or less) in the concentrations of
422 formaldehyde, acetaldehyde, acetone, acetic acid, and heptanal which however could also be
423 attributed to chamber background effects. According to TD-GCMS analysis, maleic anhydride
424 was also identified at m/z 99 in the aged emissions (Table S2).

425 Reaction with OH radicals was estimated to be the dominant daytime oxidation pathway
426 for most of the examined VOC species. For methyl vinyl ketone (m/z 71), benzene (m/z 79),
427 monoterpenes fragment (m/z 81), methyl furan (m/z 83), toluene (m/z 93), phenol (m/z 95), and
428 C8 aromatics (m/z 107, assuming o-xylene), the observed reductions in concentration were
429 close to the theoretically expected values (Table S4). Lower than predicted reductions, due to
430 OH oxidation, were observed for furan/isoprene (m/z 69; 32% less), ethyl vinyl ketone (m/z 85;
431 21% less), styrene (m/z 105; ~30% less), C9 aromatics (m/z 121; assuming 1,2,3
432 trimethylbenzene; 23% less), monoterpenes (m/z 137; assuming α -pinene; 58% less), and
433 creosol (m/z 139; 60% less). This discrepancy from theoretical predictions is likely due to the
434 presence of other compounds at the same m/z signal, including isomers, that react more slowly.
435 Ozone-induced oxidation was a minor consumption mechanism for most of the VOCs (k_{O_3}
436 ranged from 10^{-17} to $10^{-22} \text{ molecule}^{-1} \text{ cm}^3 \text{ s}^{-1}$) (Table S5), with the exception of monoterpenes
437 and their fragments (m/z 137 and 81).

438 At the end of the daytime oxidation ($t = 2 \text{ h}$), the UV lights were turned off, and nighttime
439 oxidation of the already aged emissions was conducted for two hours (2–4 h) by injecting
440 additional 80 ppb of O_3 and 130 ppb of NO_2 into the chamber. The reaction of NO_2 and O_3
441 resulted in the decrease of their levels along with production of NO_3 radical (Fig. 3d). Although



the NO_3 radical concentration was not directly measured in this study, it was estimated to range between 1 and 5×10^8 molecule cm^{-3} (typical for nighttime urban environments) based on previous dark aging experiments conducted with the same chamber setup under similar conditions (Kodros et al., 2022; Florou et al., 2023). This corresponds to approximately 4–7 hours of equivalent atmospheric exposure.

Nighttime aging led to further bbSOA production, with OA increasing by 17%, reaching $100 \mu\text{g m}^{-3}$ (Fig. 3a). Organic nitrate increased by $0.62 \mu\text{g m}^{-3}$ (72%) and total nitrate by $0.94 \mu\text{g m}^{-3}$ (53%) compared to their daytime levels. Nighttime enhancement of organic nitrate has been also reported in other studies (Kodros et al., 2020, 2022; Florou et al., 2023). The O:C ratio slightly increased from 0.58 to 0.61 (5%). A small decrease ($<1\%$) in H:C was observed, while the f_{44}/f_{60} increased further by 19% due to the nighttime oxidation. At the end of the daytime-first oxidation cycle the theta angle of the aged aerosol compared to the fresh one was 23° (Fig. 3e), suggesting significant differences. The final DTT_m of the aged emissions was $68.7 \pm 6.0 \text{ pmol min}^{-1} \mu\text{g}^{-1}$, higher by 12% compared to the daytime measured WS-OP and 34% higher than the fresh one (Table S3).

The most notable VOC increases were observed for formaldehyde (m/z 31), which increased from 1.8 to 2.2 ppb (22%); hexenal/maleic anhydride (m/z 99), which increased from 2.7 to 3.7 ppb (37%), and 2,3-benzofurandione (m/z 149), that increased from 0.2 to 0.3 ppb (50%) (Fig. S6). Further decreases in the gas-phase concentrations of furan (m/z 69) by 0.4 ppb (61%), methylfuran (m/z 95) by 0.35 ppb (26%), phenol (m/z 95) by 1.1 ppb (86%), and styrene (m/z 105) by 0.4 ppb (56%), were observed (Fig. S6).

3.4 Typical night-to-day (ND) aging experiment

ND1 is as a typical night to day oxidation experiment (Fig. 4). The initial PM_{10} concentration injected into the chamber was $121 \mu\text{g m}^{-3}$, with OA contributing 97%. The transition from fresh emissions to nighttime (0–2 h) and then daytime (2–4 h) oxidation resulted in significant changes in both the particle and gas phase. OA concentration increased by $78 \mu\text{g m}^{-3}$ (65% increase) during the nighttime oxidation and by $34 \mu\text{g m}^{-3}$ (an additional 17% increase) during daytime oxidation. During nighttime, total nitrate increased from 0.66 to $5.4 \mu\text{g m}^{-3}$, driven by production of organic nitrate. During daytime, organic nitrate levels decreased slightly (8%) compared to nighttime. The nighttime-first cycle also led to increases in ammonium levels first by $0.9 \mu\text{g m}^{-3}$ (from 0.3 to $1.2 \mu\text{g m}^{-3}$) and then by $0.3 \mu\text{g m}^{-3}$ (from 1.2 to $1.5 \mu\text{g m}^{-3}$).

The theta angle between the HR-AMS spectra of fresh and night-aged OA was 13° while at the end of the nighttime-first oxidation cycle the overall change of spectrum of the aged



aerosol compared to the fresh one was 24° (Fig. 4e), similar to that observed during the daytime-first cycle. The f_{44}/f_{60} ratio increased from 1.7 to 5.5 during night and from 5.5 to 9 during the day, while the H:C decreased from 1.67 to 1.61 and 1.58, respectively (Tables 1 and 2). The O:C increased by 34% (from 0.41 to 0.55) at night with a further 20% enhancement (from 0.55 to 0.66) observed after the day aging. DTT_m increased from $31.8 \pm 2.8 \text{ pmol min}^{-1} \mu\text{g}^{-1}$ for the fresh aerosol to $42.5 \pm 3.1 \text{ pmol min}^{-1} \mu\text{g}^{-1}$ for night-aged aerosol (36% increase) and to $71.0 \pm 5.7 \text{ pmol min}^{-1} \mu\text{g}^{-1}$ for day-aged aerosol (67% increase) (Table S3). Unlike experiment DN1, which exhibited an initial increase (daytime) followed by a decrease (nighttime) in oxidative potential, experiment ND1 showed a monotonic increase with aging (Fig. 5).

During daytime oxidation, the OH concentration was $4.2 \times 10^6 \text{ molecule cm}^{-3}$, which corresponds to approximately 5.3 h of equivalent photochemical atmospheric aging. O_3 levels increased by 88 ppb, rising from 96 ppb to 184 ppb by the end of daytime oxidation.

Similar trends and concentration levels were observed for most identified VOCs in experiments ND1 and DN1 (Fig. S6a and Fig. S7a). The observed differences in the percentage reduction of key bbSOA precursors, such as aromatic compounds and furans, between DN1 and ND1 (Fig. S6b and Fig. S7b) suggest that the variability in precursor depletion dynamics is primarily influenced by differences in oxidant availability, photochemical reactivity, and the chemical composition of the emissions.

3.5 Results of all dry daytime-first and nighttime first experiments

The average OA production (including organic nitrate) observed in the daytime-first (DN1-DN8) and nighttime-first (ND1-ND6) experiments at the end of a complete diurnal aging cycle was $51 \pm 22 \mu\text{g m}^{-3}$, ranging from 19 to $136 \mu\text{g m}^{-3}$ (Fig. 6). These values correspond to a total OA mass increase ranging from 35% to 91% compared to the fresh OA. In both oxidation cycles the majority of the produced OA was formed during the first stage of oxidation. This is consistent with the higher availability of precursor VOCs initially. No significant differences were observed in the levels of OA produced in experiments ND7 and ND8 compared to the rest (Fig. 6). This suggests that, although the use of pine kindling resulted in a different composition of fresh wood emissions, its overall impact on SOA production was less significant compared to the influence of oxidation conditions.

In some cases, the nighttime-first oxidation cycle resulted in higher SOA production (Fig. 6 and Fig. 7b). For instance, in experiment ND1, an OA mass increase of over 90% was observed at the end of the nighttime-first cycle. Similarly, in ND5, the OA increased by 78%



508 compared to fresh. Both experiments had high initial OA concentration in the fresh emissions
509 (Table 1) and higher initial O₃ levels (at around 30 ppb) compared to the rest of the nighttime-
510 first experiments, which had an average level of 14 ± 2 ppb. However, statistical analysis did
511 not confirm that the nighttime-first oxidation cycle generally leads to higher SOA production
512 compared to the daytime-first cycle.

513 During both daytime-first and nighttime-first oxidation cycles, the average density of the
514 aged aerosol increased from 1.17 to 1.33 g cm⁻³, corresponding to approximately 13% increase
515 in both cases (Table 2). Similar increases in bbSOA density, in the range of 1.31-1.34 g cm⁻³,
516 have been also reported in other chamber studies during dark aging (Li et al., 2015; Florou et
517 al., 2023).

518 At the end of the daytime-first oxidation cycle, the average O:C was 0.61 ± 0.04 , 56%
519 higher than the average O:C (0.39 ± 0.03) of the fresh bbOA in our experiments. Almost 90%
520 of this increase occurred during daytime (O:C increased from 0.39 to 0.59; Δ O:C= 0.2) (Fig.
521 7c), while the subsequent nighttime oxidation resulted in an additional 10% increase in O:C
522 (from 0.59 to 0.61). For the nighttime-first cycle, the O:C increased from 0.40 ± 0.06 for the
523 fresh emissions to 0.61 ± 0.06 (a 54% increase) at the end of the cycle (Fig. 7d). In this case,
524 the contributions of the nighttime and daytime oxidation stages to the increase in O:C were
525 almost equal, at 55% and 45%, respectively. In both oxidation cycles the final O:C is similar,
526 but the importance of each oxidation stage depends on the order (oxidation sequence).

527 In all experiments, the OA AMS spectra changed progressively with aging. The
528 predominant differences between the average fresh and aged bbSOA spectra at the end of
529 daytime-first cycle were found for m/z 28 (more than 2-fold increase) and 44 (1.5-fold increase)
530 (Fig. S2). Significant decreases were observed for m/z 60 (37%) and 91 (36%), 115 (38%) and
531 137 (42%). The same changes were observed comparing the fresh and the nighttime-first aged
532 bbSOA (Fig. S2). During the daytime-first cycles the main changes in the OA spectrum
533 occurred during the first (daytime) oxidation regime, with a theta angle of $26 \pm 4^\circ$ on average
534 (Fig. 7e). The further change in the second step (nighttime) was $4 \pm 2^\circ$ on average. In contrast,
535 a more balanced change was observed in the evolution of the theta angle over time during the
536 nighttime-first cycle (Fig. 7f). The average OA spectrum shifted by $19 \pm 4^\circ$ on average during
537 nighttime, followed by an additional 10° shift during UV exposure. Overall, at the end of both
538 cycles, regardless of the followed oxidation path, the final average bbSOA spectra were almost
539 identical ($\theta < 3^\circ$) (Fig. 8).

540 To evaluate the environmental relevance of the chamber-produced bbSOA, the final
541 daytime-first and nighttime-first bbSOA spectra from this study were compared to the spectra



542 of oxidized OA, that was measured at a remote site in Greece (Pertouli) during the summer of
543 2022 (Vasilakopoulou et al., 2023). Most of this aged OA was aged emissions of wildfires from
544 different regions of Europe. Two oxygenated OA (OOA) factors; a more-oxidized OOA (MO-
545 OOA) and a less-oxidized OOA (LO-OOA) were needed to reproduce the observed OA
546 spectra. Our final bbSOA spectra showed greater similarity to the LO-OOA factor, with a theta
547 angle of approximately 16° , and were more distinct (θ at around 30°) from the MO-OOA
548 spectra measured in Pertouli. This suggests that our experiments simulated the earlier stages of
549 atmospheric aging, while additional aging processes likely occur under ambient conditions (see
550 also Fig. S8).

551 Changes in VOC levels of aged emissions across all daytime first (Fig. S9) and nighttime-
552 first (Fig. S10) experiments were consistent with those observed in the typical experiments
553 DN1 and ND1. Both aging cycles resulted in a significant decrease in the concentration of
554 furans and their derivatives, cyclic and polycyclic aromatic hydrocarbons and terpenes. The
555 day aged Tenax samples indicated a moderate decrease in aromatic species like toluene (~20%)
556 and benzene, which is consistent with their lower reaction rates compared to higher carbon
557 number aromatics. Rapid decrease in concentration was noted for species like phenol (~45%)
558 and furfural (~75%), as well as their structurally related compounds. Related products,
559 including 2-nitro-phenol, 4-methyl-2-nitro-phenol, maleic anhydride, and 3-methyl-2,5-
560 furandione, were also detected. p-Benzoquinone was also formed, possibly as a result of the
561 reacted aromatics. Benzofuran was absent from the aged samples; instead, 2,3-
562 benzofurandione was detected. At the same time a progressive increase in aldehydes and
563 ketones was observed, along with significant increases in carboxylic acids, such as formic (m/z
564 47) and acetic (m/z 61). The benzaldehyde concentration increased, accompanied by the
565 formation of benzeneacetaldehyde, 2-hydroxy-benzaldehyde, 3-ethyl-benzaldehyde. A notable
566 increase in butanol was also observed in the Tenax samples, along with the formation of
567 straight-chain aldehydes (hexanal to undecanal). The GC-MS measurements for the night-aged
568 samples following daytime processing were consistent with those of the PTR-MS. Furfural was
569 no longer detected, while a further decrease in phenol and increases in benzaldehyde and
570 butanol were noted. A cumulative depiction of the experiment's progression in terms of
571 oxidation and VOCs detected by the GC-MS, is provided in Fig. S11. Similar results were
572 obtained for the other experiments.



573 **3.6 Effect of daytime-first and nighttime-first oxidation cycle on WS-OP**

574 The water-soluble oxidative potential (WS-OP) of fresh emissions ranged from $21 \text{ pmol min}^{-1} \mu\text{g}^{-1}$
575 μg^{-1} to $79 \text{ pmol min}^{-1} \mu\text{g}^{-1}$ and that of aged wood-burning emissions from $39 \text{ pmol min}^{-1} \mu\text{g}^{-1}$
576 to $127 \text{ pmol min}^{-1} \mu\text{g}^{-1}$ (Table S3). These values fall within the range reported in literature for
577 fresh bbOA and aged bbOA (Verma et al., 2015; Tuet et al., 2017; Bates et al., 2019;
578 Daellenbach et al., 2020; Wang et al., 2023).

579 The evolution of average WS-OP of fresh and aged emissions, considering all
580 experiments and both oxidation cycles, (Fig. 9) was similar to that observed in experiments
581 DN1 and DN1 (Fig. 5). The average WS-OP values for the daytime-first cycle were $47.9 \pm$
582 $17.7 \text{ pmol min}^{-1} \mu\text{g}^{-1}$ for fresh emissions, $93 \pm 27 \text{ pmol min}^{-1} \mu\text{g}^{-1}$ for daytime-aged emissions,
583 representing a 94% increase compared to fresh aerosol, and $73.4 \pm 13.3 \text{ pmol min}^{-1} \mu\text{g}^{-1}$ for
584 nighttime-aged emissions, indicating a 21% reduction compared to daytime-aged WS-OP (Fig.
585 9a). For the nighttime-first oxidation cycle, the average WS-OP of the fresh emissions were
586 $37.8 \pm 10.6 \text{ pmol min}^{-1} \mu\text{g}^{-1}$. After nighttime aging, it increased by 44% to $54.4 \pm 13.6 \text{ pmol}$
587 $\text{min}^{-1} \mu\text{g}^{-1}$, and following daytime aging, it further increased by $62.9 \pm 20.4 \text{ pmol min}^{-1} \mu\text{g}^{-1}$
588 (Fig. 9b).

589 Statistical analysis (t-test) showed that aged WS-OP values were significantly higher than
590 those of fresh emissions in all experiments, for both oxidation cycles. Additionally, for the
591 daytime-first oxidation cycle, a statistically significant difference was observed between the
592 WS-OP of nighttime-aged (NO_3 -oxidized) and daytime-aged (UV-oxidized) emissions.
593 Further details on the statistical analysis are provided in Supplementary Section S4 and Table
594 S9.

595 The overall increase in WS-OP at the end of the two oxidation cycles was $53 \pm 34\%$ for
596 the daytime-first cycle and $66 \pm 8\%$ for the nighttime-first cycle, indicating that both daytime
597 and nighttime aging of biomass burning emissions consistently enhanced their oxidative
598 potential. Our results suggest that the sequence of chemical processes – whether the emissions
599 are first oxidized by OH or NO_3 – can significantly affect the temporal evolution of OP. This,
600 in turn, may also influence the health impacts associated with exposure to biomass burning
601 plumes, depending on the time of day when the emissions occur. Although daytime boundary
602 layer dynamics generally favour mixing and dilution of pollutants, daytime burning in urban
603 environments may actually be as or more aggravating than nighttime burning, owing to the
604 enhanced oxidative processing of the emissions occurring in the former stage of the diurnal
605 cycle.



606 The correlation of WS-OP with produced OA and degree of oxidation (O:C) were also
607 investigated. Three OA types were considered (fresh, day-aged, and night-aged). WS-OP was
608 not well correlated with either the O:C ratio ($R^2 < 30\%$) of the organic aerosol or its fresh and
609 aged fractions (R^2 up to 34%) (Fig. S12). This implies that the link between bbOA aging, and
610 WS-OP change is complex and cannot be just described by one variable.

611 The observed WS-OP trends could be linked to the VOC composition and oxidation
612 processes in the daytime-first and nighttime-first cycles. The daytime-first cycle exhibits a high
613 daytime WS-OP due to the OH oxidation of VOCs such as furans, aromatics, and phenolic
614 compounds, leading to the formation of reactive species like, 4-methyl-2-nitrophenol, and
615 highly reactive p-benzoquinone. In contrast, the nighttime-first cycle shows a gradual increase
616 in WS-OP. After one complete diurnal cycle, WS-OP values in both cycles converge,
617 indicating that oxidative processes in both pathways ultimately lead to similar levels of
618 oxidation products. This convergence highlights the role of both fast and slow oxidation
619 mechanisms in determining aerosol OP and suggests that even VOCs with lower reactivity can
620 significantly contribute to aerosol toxicity over extended atmospheric aging.

621 4 Conclusions

622 This study investigated how different diurnal oxidation sequences, daytime-first and
623 nighttime-first, affect the formation of OA, the gas-phase composition, and the oxidative
624 potential of emissions produced by burning olive wood and olive wood mixed with pine
625 throughout a complete diurnal aging cycle. Both daytime-first and nighttime-first oxidation
626 cycles resulted in enhancement in OA levels by 35%-90%. The mixture of olive wood with
627 pine kindling resulted in a different composition of fresh emissions; however, its overall impact
628 on SOA production was less significant compared to the influence of oxidation conditions.

629 The daytime-first cycle favoured rapid daytime oxidation, producing highly oxygenated
630 species and increasing the O:C ratio of the fresh emissions from 0.39 ± 0.04 to 0.59 ± 0.04
631 during daytime, reaching finally at 0.61 ± 0.03 during nighttime. The nighttime-first cycle
632 showed a gradual (two-steps) oxidation increase with a similar final O:C ratio of 0.61 ± 0.06 .
633 The daytime-first cycle exhibited rapid spectral changes during daytime oxidation, while
634 nighttime-first cycles showed a more balanced two-step evolution. At the end of both cycles,
635 the final average bbSOA spectra were nearly identical ($R^2 > 0.99$; $\theta < 3^\circ$), indicating that the
636 aerosol was transformed into similar aged OA regardless of the initial oxidation step (daytime
637 or nighttime) at the start of the cycle. The chamber-produced bbSOA resembled the less-
638 oxidized OOA in a field campaign in Greece with the corresponding OA dominated by aged



639 bbOA, suggesting that the present study has addressed only part of the aging that occurs in the
640 atmosphere.

641 Both the daytime-first and nighttime-first oxidation cycles effectively reduced the
642 concentration of bbSOA precursors (e.g., furans, aromatic hydrocarbons, terpenes).
643 Concurrently, a progressive increase in aldehydes and ketones was observed in both cycles,
644 alongside increases in carboxylic acids, such as formic and acetic acids. The daytime-first cycle
645 resulted in a $53 \pm 34\%$ increase in WS-OP of aerosol while the nighttime-first cycle showed a
646 slightly higher increase of $66 \pm 8\%$. The final WS-OP values of the daytime-first (73 ± 14 pmol
647 $\text{min}^{-1} \mu\text{g}^{-1}$) and nighttime-first (63 ± 20 pmol $\text{min}^{-1} \mu\text{g}^{-1}$) cycles were statistically similar.

648 These findings underscore the importance of considering oxidation sequences when
649 assessing the environmental fate and health impacts of biomass burning emissions. This
650 highlights the complex and dynamic nature of atmospheric aging processes. Future research
651 should investigate the effects of prolonged atmospheric aging under more realistic conditions,
652 such as higher initial relative humidity, multiple day-night cycles, and conduct detailed
653 chemical analyses of particle-phase products to better understand contributions of specific
654 chemical components to aerosol OP.

655 **Author contributions**

656 M.P.G., K.F., and A.M. contributed to investigation, conducted the experiments and performed
657 the laboratory measurements.; M.P.G. and G.S. performed the offline measurement of the
658 water-soluble oxidative potential of the collected aerosol samples.; A.M. performed the offline
659 TD-GCMS analysis of the Tenax samples; C.K. contributed to chamber set-up optimization.;
660 A.N. conceived and supported the research project; S.N.P. supported and directed this
661 research.; M.P.G. and K.F. interpreted the results and contributed to formal data analysis;
662 M.P.G. wrote the original manuscript with contributions from all co-authors.; All authors
663 contributed to the review and editing of the manuscript and have approved the final submitted
664 version.

665 **Conflicts of interest**

666 The authors declare that there are no conflicts to declare.

667 **Funding information**

668 This work was supported by the project NANOSOMs (Grant 11504) of the Greek HFRI, the
669 Horizon 2020 project REMEDIA (grant agreement no. 874753), and the European Research
670 Council (ERC) under the European Union's Horizon 2020 research and innovation programme
671 (grant agreement no. 726165, PyroTRACH – Pyrogenic Transformations Affecting Climate
672 and Health).

673



674 5 References

- 675 Allani, A., Bedjanian, Y., Papanastasiou, D. K., and Romanias, M. N.: Reaction rate
676 coefficient of OH radicals with d₉-butanol as a function of temperature, *ACS Omega*, 6,
677 18123–18134, <https://doi.org/10.1021/acsomega.1c01942>, 2021.
- 678 Alper, K., Tekin, K., Karagöz, S., and Ragauskas, A. J.: Sustainable energy and fuels from
679 biomass: a review focusing on hydrothermal biomass processing, *Sustain. Energy Fuels*,
680 4, 4390–4414, <https://doi.org/10.1039/d0se00784f>, 2020.
- 681 Barmet, P., Dommen, J., DeCarlo, P. F., Tritscher, T., Praplan, A. P., Platt, S. M., Prévôt, A.
682 S. H., Donahue, N. M., and Baltensperger, U.: OH clock determination by proton
683 transfer reaction mass spectrometry at an environmental chamber, *Atmos. Meas. Tech.*,
684 5, 647–656, <https://doi.org/10.5194/amt-5-647-2012>, 2012.
- 685 Bates, J. T., Fang, T., Verma, V., Zeng, L., Weber, R. J., Tolbert, P. E., Abrams, J. Y., Sarnat,
686 S. E., Klein, M., Mulholland, J. A., and Russell, A. G.: Review of Acellular Assays of
687 Ambient Particulate Matter Oxidative Potential: Methods and Relationships with
688 Composition, Sources, and Health Effects, *Environ Sci Technol*, 53, 4003–4019,
689 <https://doi.org/10.1021/ACS.EST.8B03430>, 2019.
- 690 Bray, C. D., Battye, W. H., Aneja, V. P., and Schlesinger, W. H.: Global emissions of NH₃,
691 NO_x, and N₂O from biomass burning and the impact of climate change, *J. Air Waste*
692 *Manage. Assoc.*, 71, 102–114, <https://doi.org/10.1080/10962247.2020.1842822>, 2021.
- 693 Briggs, N. L., Jaffe, D. A., Gao, H., Hee, J. R., Baylon, P. M., Zhang, Q., Zhou, S., Collier, S.
694 C., Sampson, P. D., and Cary, R. A.: Particulate matter, ozone, and nitrogen species in
695 aged wildfire plumes observed at the mount bachelor observatory, *Aerosol Air Qual.*
696 *Res.*, 16, 3075–3087, <https://doi.org/10.4209/aaqr.2016.03.0120>, 2016.
- 697 Bruns, E. A., Slowik, J. G., El Haddad, I., Kilic, D., Klein, F., Dommen, J., Temime-Roussel,
698 B., Marchand, N., Baltensperger, U., and Prévôt, A. S. H.: Characterization of gas-phase
699 organics using proton transfer reaction time-of-flight mass spectrometry: fresh and aged
700 residential wood combustion emissions, *Atmos. Chem. Phys.*, 17, 705–720,
701 <https://doi.org/10.5194/acp-17-705-2017>, 2017.
- 702 Canagaratna, M. R., Jimenez, J. L., Kroll, J. H., Chen, Q., Kessler, S. H., Massoli, P.,
703 Hildebrandt Ruiz, L., Fortner, E., Williams, L. R., Wilson, K. R., Surratt, J. D.,
704 Donahue, N. M., Jayne, J. T., and Worsnop, D. R.: Elemental ratio measurements of
705 organic compounds using aerosol mass spectrometry: characterization, improved
706 calibration, and implications, *Atmos. Chem. Phys.*, 15, 253–272,
707 <https://doi.org/10.5194/acp-15-253-2015>, 2015.
- 708 Cao, T., Li, M., Zou, C., Fan, X., Song, J., Jia, W., Yu, C., Yu, Z., and Peng, P.: Chemical
709 composition, optical properties, and oxidative potential of water-and methanol-soluble
710 organic compounds emitted from the combustion of biomass materials and coal, *Atmos.*
711 *Chem. Phys.*, 21, 13187–13205, <https://doi.org/10.5194/acp-21-13187-2021>, 2021.
- 712 Cappa, C. D., Lim, C. Y., Hagan, D. H., Coggon, M., Koss, A., Sekimoto, K., De Gouw, J.,
713 Onasch, T. B., Warneke, C., and Kroll, J. H.: Biomass-burning-derived particles from a
714 wide variety of fuels-Part 2: Effects of photochemical aging on particle optical and
715 chemical properties, *Atmos. Chem. Phys.*, 20, 8511–8532, <https://doi.org/10.5194/acp-20-8511-2020>, 2020.



- 717 Che, H., Segal-Rozenhaimer, M., Zhang, L., Dang, C., Zuidema, P., Dobracki, A., Sedlacek,
718 A. J., Coe, H., Wu, H., Taylor, J., Zhang, X., Redemann, J., and Haywood, J.: Cloud
719 processing and weeklong ageing affect biomass burning aerosol properties over the
720 south-eastern Atlantic, *Commun. Earth Environ.*, 3, 182, [https://doi.org/10.1038/s43247-](https://doi.org/10.1038/s43247-022-00517-3)
721 022-00517-3, 2022.
- 722 Chen, G., Canonaco, F., Tobler, A., Aas, W., Alastuey, A., Allan, J., Atabakhsh, S., Aurela,
723 M., Baltensperger, U., Bougiatioti, A., De Brito, J. F., Ceburnis, D., Chazeau, B.,
724 Chebaicheb, H., Daellenbach, K. R., Ehn, M., El Haddad, I., Eleftheriadis, K., Favez,
725 O., Flentje, H., Font, A., Fossum, K., Freney, E., Gini, M., Green, D. C., Heikkinen, L.,
726 Herrmann, H., Kalogridis, A. C., Keernik, H., Lhotka, R., Lin, C., Lunder, C.,
727 Maasikmets, M., Manousakas, M. I., Marchand, N., Marin, C., Marmureanu, L.,
728 Mihalopoulos, N., Močnik, G., Nęcki, J., O'Dowd, C., Ovadnevaite, J., Peter, T., Petit,
729 J. E., Pikridas, M., Matthew Platt, S., Pokorná, P., Poulain, L., Priestman, M., Riffault,
730 V., Rinaldi, M., Róžański, K., Schwarz, J., Sciare, J., Simon, L., Skiba, A., Slowik, J.
731 G., Sosedova, Y., Stavroulas, I., Styszko, K., Teinmaa, E., Timonen, H., Tremper, A.,
732 Vasilescu, J., Via, M., Vodička, P., Wiedensohler, A., Zografou, O., Cruz Minguiñón,
733 M., and Prévôt, A. S. H.: European aerosol phenomenology - 8: Harmonised source
734 apportionment of organic aerosol using 22 year-long ACSM/AMS datasets, *Environ. Int.*
735 166, 107325, <https://doi.org/10.1016/j.envint.2022.107325>, 2022.
- 736 Cho, A. K., Sioutas, C., Miguel, A. H., Kumagai, Y., Schmitz, D. A., Singh, M., Eiguren-
737 Fernandez, A., and Froines, J. R.: Redox activity of airborne particulate matter at
738 different sites in the Los Angeles Basin, *Environ. Res.*, 99, 40–47,
739 <https://doi.org/10.1016/j.envres.2005.01.003>, 2005.
- 740 Cincinelli, A., Guerranti, C., Martellini, T., and Scodellini, R.: Residential wood combustion
741 and its impact on urban air quality in Europe, *Curr. Opin. Environ. Sci. Health*, 8, 10–
742 14, <https://doi.org/10.1016/j.coesh.2018.12.007>, 2019.
- 743 Costabile, F., Gualtieri, M., Rinaldi, M., Canepari, S., Vecchi, R., Massimi, L., Di Iulio, G.,
744 Paglione, M., Di Liberto, L., Corsini, E., Facchini, M. C., and Decesari, S.: Exposure to
745 urban nanoparticles at low PM₁ concentrations as a source of oxidative stress and
746 inflammation, *Sci. Rep.*, 13, 1–18, <https://doi.org/10.1038/s41598-023-45230-z>, 2023.
- 747 Daellenbach, K. R., Uzu, G., Jiang, J., Cassagnes, L. E., Leni, Z., Vlachou, A., Stefanelli, G.,
748 Canonaco, F., Weber, S., Segers, A., Kuenen, J. J. P., Schaap, M., Favez, O., Albinet,
749 A., Aksoyoglu, S., Dommen, J., Baltensperger, U., Geiser, M., El Haddad, I., Jaffrezo, J.
750 L., and Prévôt, A. S. H.: Sources of particulate-matter air pollution and its oxidative
751 potential in Europe, *Nature*, 587, 414–419, <https://doi.org/10.1038/S41586-020-2902-8>,
752 2020.
- 753 Desservettaz, M., Pikridas, M., Stavroulas, I., Bougiatioti, A., Liakakou, E., Hatzianastassiou,
754 N., Sciare, J., Mihalopoulos, N., and Bourtsoukidis, E.: Emission of volatile organic
755 compounds from residential biomass burning and their rapid chemical transformations,
756 *Sci. Total Environ.*, 903, 166592, <https://doi.org/10.1016/j.scitotenv.2023.166592>, 2023.
- 757 Dominutti, P. A., Jaffrezo, J.-L., Marsal, A., Mhadhbi, T., Elazzouzi, R., Rak, C., Cavalli, F.,
758 Putaud, J.-P., Bougiatioti, A., Mihalopoulos, N., Paraskevopoulou, D., Mudway, I.,
759 Nenes, A., Daellenbach, K. R., Banach, C., Campbell, S. J., Cigánková, H., Contini, D.,
760 Evans, G., Georgopoulou, M., Ghanem, M., Glencross, D. A., Guascito, M. R.,
761 Herrmann, H., Iram, S., Jovanović, M., Jovašević-Stojanović, M., Kalberer, M., Kooter,



- 762 I. M., Paulson, S. E., Patel, A., Perdrix, E., Pietrogrande, M. C., Mikuška, P., Sauvain,
763 J.-J., Seitanidi, K., Shahpoury, P., Souza, E. J. d. S., Steimer, S., Stevanovic, S., Suarez,
764 G., Subramanian, P. S. G., Uttinger, B., van Os, M. F., Verma, V., Wang, X., Weber, R.
765 J., Yang, Y., Querol, X., Hoek, G., Harrison, R. M., and Uzu, G.: An interlaboratory
766 comparison to quantify oxidative potential measurement in aerosol particles: challenges
767 and recommendations for harmonisation, *Atmos. Meas. Tech.*, 18, 177–195,
768 <https://doi.org/10.5194/AMT-18-177-2025>, 2025.
- 769 Donahue, N. M., Henry, K. M., Mentel, T. F., Kiendler-Scharr, A., Spindler, C., Bohn, B.,
770 Brauers, T., Dorn, H. P., Fuchs, H., Tillmann, R., Wahner, A., Saathoff, H., Naumann,
771 K. H., Möhler, O., Leisner, T., Müller, L., Reinnig, M. C., Hoffmann, T., Salo, K.,
772 Hallquist, M., Frosch, M., Bilde, M., Tritscher, T., Barmet, P., Praplan, A. P., DeCarlo,
773 P. F., Dommen, J., Prévôt, A. S. H., and Baltensperger, U.: Aging of biogenic secondary
774 organic aerosol via gas-phase OH radical reactions, *Proc. Natl. Acad. Sci. U.S.A.*, 109
775 (34), 13503–13508, <https://doi.org/10.1073/pnas.1115186109>, 2012.
- 776 Fachinger, F., Drewnick, F., Gieré, R., and Borrmann, S.: How the user can influence
777 particulate emissions from residential wood and pellet stoves: Emission factors for
778 different fuels and burning conditions, *Atmos. Environ.*, 158, 216–226,
779 <https://doi.org/10.1016/j.atmosenv.2017.03.027>, 2017.
- 780 Fang, T., Verma, V., Guo, H., King, L. E., Edgerton, E. S., and Weber, R. J.: A semi-
781 automated system for quantifying the oxidative potential of ambient particles in aqueous
782 extracts using the dithiothreitol (DTT) assay: results from the Southeastern Center for
783 Air Pollution and Epidemiology (SCAPE), *Atmos. Meas. Tech.*, 8, 471–482,
784 <https://doi.org/10.5194/amt-8-471-2015>, 2015.
- 785 Fang, Z., Li, C., He, Q., Czech, H., Gröger, T., Zeng, J., Fang, H., Xiao, S., Pardo, M.,
786 Hartner, E., Meidan, D., Wang, X., Zimmermann, R., Laskin, A., and Rudich, Y.:
787 Secondary organic aerosols produced from photochemical oxidation of secondarily
788 evaporated biomass burning organic gases: Chemical composition, toxicity, optical
789 properties, and climate effect, *Environ Int.*, 157,
790 <https://doi.org/10.1016/J.ENVINT.2021.106801>, 2021.
- 791 Florou, K., Kodros, J. K., Paglione, M., Jorga, S., Squizzato, S., Masiol, M., Uruci, P., Nenes,
792 A., and Pandis, S. N.: Characterization and dark oxidation of the emissions of a pellet
793 stove, *Environ. Sci.: Atmos.*, 3, 1319–1334, <https://doi.org/10.1039/d3ea00070b>, 2023.
- 794 Fry, J. L., Draper, D. C., Barsanti, K. C., Smith, J. N., Ortega, J., Winkler, P. M., Lawler, M.
795 J., Brown, S. S., Edwards, P. M., Cohen, R. C., and Lee, L.: Secondary organic aerosol
796 formation and organic nitrate yield from NO₃ oxidation of biogenic hydrocarbons,
797 *Environ. Sci. Technol.*, 48, 11944–11953, <https://doi.org/10.1021/es502204x>, 2014.
- 798 Gao, D., Ripley, S., Weichenthal, S., and Godri Pollitt, K. J.: Ambient particulate matter
799 oxidative potential: Chemical determinants, associated health effects, and strategies for
800 risk management, *Free Radic. Biol. Med.*, 151, 7–25,
801 <https://doi.org/10.1016/j.freeradbiomed.2020.04.028>, 2020.
- 802 Guercio, V., Pojum, I. C., Leonardi, G. S., Shrubsole, C., Gowers, A. M., Dimitroulopoulou,
803 S., and Exley, K. S.: Exposure to indoor and outdoor air pollution from solid fuel
804 combustion and respiratory outcomes in children in developed countries: a systematic
805 review and meta-analysis, *Sci. Total Environ.*, 755, 142187,
806 <https://doi.org/10.1016/j.scitotenv.2020.142187>, 2021.



- 807 Harshman, S. W., Mani, N., Geier, B. A., Kwak, J., Shepard, P., Fan, M., Sudberry, G. L.,
808 Mayes, R. S., Ott, D. K., Martin, J. A., and Grigsby, C. C.: Storage stability of exhaled
809 breath on Tenax TA, *J. Breath Res.*, 10, 046008, [https://doi.org/10.1088/1752-](https://doi.org/10.1088/1752-7155/10/4/046008)
810 7155/10/4/046008, 2016.
- 811 Hartikainen, A., Yli-Pirilä, P., Tiitta, P., Leskinen, A., Kortelainen, M., Orasche, J., Schnelle-
812 Kreis, J., Lehtinen, K. E. J., Zimmermann, R., Jokiniemi, J., and Sippula, O.: Volatile
813 organic compounds from logwood combustion: emissions and transformation under dark
814 and photochemical aging conditions in a smog chamber, *Environ. Sci. Technol.*, 52,
815 4979–4988, <https://doi.org/10.1021/acs.est.7b06269>, 2018.
- 816 He, L. Y., Lin, Y., Huang, X. F., Guo, S., Xue, L., Su, Q., Hu, M., Luan, S. J., and Zhang, Y.
817 H.: Characterization of high-resolution aerosol mass spectra of primary organic aerosol
818 emissions from Chinese cooking and biomass burning, *Atmos. Chem. Phys.*, 10, 11535–
819 11543, <https://doi.org/10.5194/ACP-10-11535-2010>, 2010.
- 820 He, Y., Zhao, B., Wang, S., Valorso, R., Chang, X., Yin, D., Feng, B., Camredon, M.,
821 Aumont, B., Dearden, A., Jathar, S. H., Shrivastava, M., Jiang, Z., Cappa, C. D., Yee, L.
822 D., Seinfeld, J. H., Hao, J., and Donahue, N. M.: Formation of secondary organic
823 aerosol from wildfire emissions enhanced by long-time ageing, *Nat. Geosci.*, 17, 124–
824 129, <https://doi.org/10.1038/s41561-023-01355-4>, 2024.
- 825 Hennigan, C. J., Miracolo, M. A., Engelhart, G. J., May, A. A., Presto, A. A., Lee, T.,
826 Sullivan, A. P., McMeeking, G. R., Coe, H., Wold, C. E., Hao, W. M., Gilman, J. B.,
827 Kuster, W. C., De Gouw, J., Schichtel, B. A., Collett, J. L., Kreidenweis, S. M., and
828 Robinson, A. L.: Chemical and physical transformations of organic aerosol from the
829 photo-oxidation of open biomass burning emissions in an environmental chamber,
830 *Atmos. Chem. Phys.*, 11, 7669–7686, <https://doi.org/10.5194/acp-11-7669-2011>, 2011.
- 831 Hodshire, A. L., Akherati, A., Alvarado, M. J., Brown-Steiner, B., Jathar, S. H., Jimenez, J.
832 L., Kreidenweis, S. M., Lonsdale, C. R., Onasch, T. B., Ortega, A. M., and Pierce, J. R.:
833 Aging effects on biomass burning aerosol mass and composition: a critical review of
834 field and laboratory studies., *Environ. Sci. Technol.*, 53, 10007–10022,
835 <https://doi.org/10.1021/acs.est.9b02588>, 2019.
- 836 Huang, G., Wang, S., Chang, X., Cai, S., Zhu, L., Li, Q., and Jiang, J.: Emission factors and
837 chemical profile of I/SVOCs emitted from household biomass stove in China, *Sci. Total*
838 *Environ.*, 842, 156940, <https://doi.org/10.1016/j.scitotenv.2022.156940>, 2022.
- 839 IEA: Key World Energy Statistics 2019, OECD Publishing, Paris,
840 <https://doi.org/10.1787/71b3ce84-en>, 2019.
- 841 IEA: Key World Energy Statistics 2021, OECD Publishing, Paris,
842 <https://doi.org/10.1787/2ef8cebc-en>, 2021.
- 843 Jiang, K., Xing, R., Luo, Z., Huang, W., Yi, F., Men, Y., Zhao, N., Chang, Z., Zhao, J., Pan,
844 B., and Shen, G.: Pollutant emissions from biomass burning: A review on emission
845 characteristics, environmental impacts, and research perspectives, *Particuology*, 85,
846 296–309, <https://doi.org/10.1016/j.partic.2023.07.012>, 2024.
- 847 Jorga, S. D., Kaltsonoudis, C., Liangou, A., and Pandis, S. N.: Measurement of formation
848 rates of secondary aerosol in the ambient urban atmosphere using a dual smog chamber
849 system, *Environ. Sci. Technol.*, 54, 1336–1343, <https://doi.org/10.1021/acs.est.9b03479>,
850 2020.



- 851 Jorga, S. D., Florou, K., Kaltsonoudis, C., Kodros, J. K., Vasilakopoulou, C., Cirtog, M.,
852 Fouqueau, A., Picquet-Varrault, B., Nenes, A., and Pandis, S. N.: Nighttime chemistry
853 of biomass burning emissions in urban areas: A dual mobile chamber study, *Atmos.*
854 *Chem. Phys.*, 21, 15337–15349, <https://doi.org/10.5194/acp-21-15337-2021>, 2021.
- 855 Kaltsonoudis, C., Kostenidou, E., Florou, K., Psichoudaki, M., and Pandis, S. N.: Temporal
856 variability and sources of VOCs in urban areas of the eastern Mediterranean, *Atmos.*
857 *Chem. Phys.*, 16, 14825–14842, <https://doi.org/10.5194/acp-16-14825-2016>, 2016.
- 858 Kiendler-Scharr, A., Mensah, A. A., Friese, E., Topping, D., Nemitz, E., Prevot, A. S. H.,
859 Äijälä, M., Allan, J., Canonaco, F., Canagaratna, M., Carbone, S., Crippa, M., Dall'Osto,
860 M., Day, D. A., De Carlo, P., Di Marco, C. F., Elbern, H., Eriksson, A., Freney, E., Hao,
861 L., Herrmann, H., Hildebrandt, L., Hillamo, R., Jimenez, J. L., Laaksonen, A.,
862 McFiggans, G., Mohr, C., O'Dowd, C., Otjes, R., Ovadnevaite, J., Pandis, S. N.,
863 Poulain, L., Schlag, P., Sellegri, K., Swietlicki, E., Tiitta, P., Vermeulen, A., Wahner,
864 A., Worsnop, D., and Wu, H. C.: Ubiquity of organic nitrates from nighttime chemistry
865 in the European submicron aerosol, *Geophys. Res. Lett.*, 43, 7735–7744,
866 <https://doi.org/10.1002/2016gl069239>, 2016.
- 867 Kodros, J. K., Papanastasiou, D. K., Paglione, M., Masiol, M., Squizzato, S., Florou, K.,
868 Skyllakou, K., Kaltsonoudis, C., Nenes, A., and Pandis, S. N.: Rapid dark aging of
869 biomass burning as an overlooked source of oxidized organic aerosol, *Proc. Natl. Acad.*
870 *Sci. USA*, 117, 33028–33033, <https://doi.org/10.1073/pnas.2010365117>, 2020.
- 871 Kodros, J. K., Kaltsonoudis, C., Paglione, M., Florou, K., Jorga, S., Vasilakopoulou, C.,
872 Cirtog, M., Cazaunau, M., Picquet-Varrault, B., Nenes, A., and Pandis, S. N.: Secondary
873 aerosol formation during the dark oxidation of residential biomass burning emissions,
874 *Environ. Sci.: Atmos.*, 2, 1221–1236, <https://doi.org/10.1039/d2ea00031h>, 2022.
- 875 Kostenidou, E., Pathak, R. K., and Pandis, S. N.: An algorithm for the calculation of
876 secondary organic aerosol density combining AMS and SMPS data, *Aerosol Sci.*
877 *Technol.*, 41, 1002–1010, <https://doi.org/10.1080/02786820701666270>, 2007.
- 878 Kostenidou, E., Lee, B. H., Engelhart, G. J., Pierce, J. R., and Pandis, S. N.: Mass spectra
879 deconvolution of low, medium, and high volatility biogenic secondary organic aerosol,
880 *Environ. Sci. Technol.*, 43, 4884–4889, <https://doi.org/10.1021/es803676g>, 2009.
- 881 Kuwata, M., Zorn, S. R., and Martin, S. T.: Using elemental ratios to predict the density of
882 organic material composed of carbon, hydrogen, and oxygen, *Environ. Sci. Technol.*, 46,
883 787–794, <https://doi.org/10.1021/es202525q>, 2012.
- 884 Lei, R., Wei, Z., Chen, M., Meng, H., Wu, Y., and Ge, X.: Aging effects on the toxicity
885 alteration of different types of organic aerosols: a review, *Curr. Pollut. Rep.*, 1, 1–12,
886 <https://doi.org/10.1007/s40726-023-00272-9>, 2023.
- 887 Li, C., Ma, Z., Chen, J., Wang, X., Ye, X., Wang, L., Yang, X., Kan, H., Donaldson, D. J.,
888 and Mellouki, A.: Evolution of biomass burning smoke particles in the dark, *Atmos*
889 *Environ.*, 120, 244–252, <https://doi.org/10.1016/j.atmosenv.2015.09.003>, 2015.
- 890 Li, J., Li, J., Wang, G., Ho, K. F., Dai, W., Zhang, T., Wang, Q., Wu, C., Li, L., Li, L., and
891 Zhang, Q.: Effects of atmospheric aging processes on in vitro induced oxidative stress
892 and chemical composition of biomass burning aerosols, *J. Hazard. Mater.*, 401, 123750,
893 <https://doi.org/10.1016/j.jhazmat.2020.123750>, 2021.
- 894 Li, K., Zhang, J., Bell, D. M., Wang, T., Lamkaddam, H., Cui, T., Qi, L., Surdu, M., Wang,
895 D., Du, L., Haddad, I. El, Slowik, J. G., and Prevot, A. S. H.: Uncovering the dominant



- 896 contribution of intermediate volatility compounds in secondary organic aerosol
897 formation from biomass-burning emissions, *Natl. Sci. Rev.*, 11,
898 <https://doi.org/10.1093/NSR/NWAE014>, 2024.
- 899 Li, S., Liu, D., Wu, Y., Hu, K., Jiang, X., Tian, P., Sheng, J., Pan, B., and Zhao, D.: Aging
900 effects on residential biomass burning emissions under quasi-real atmospheric
901 conditions, *Environ. Pollut.*, 337, 122615, <https://doi.org/10.1016/j.envpol.2023.122615>,
902 2023.
- 903 Lim, C. Y., Hagan, D. H., Coggon, M. M., Koss, A. R., Sekimoto, K., De Gouw, J.,
904 Warneke, C., Cappa, C. D., and Kroll, J. H.: Secondary organic aerosol formation from
905 the laboratory oxidation of biomass burning emissions, *Atmos. Chem. Phys.*, 19, 12797–
906 12809, <https://doi.org/10.5194/acp-19-12797-2019>, 2019.
- 907 Lim, H., Silvergren, S., Spinicci, S., Mashayekhy Rad, F., Nilsson, U., Westerholm, R., and
908 Johansson, C.: Contribution of wood burning to exposures of PAHs and oxy-PAHs in
909 Eastern Sweden, *Atmos. Chem. Phys.*, 22, 11359–11379, <https://doi.org/10.5194/acp-22-11359-2022>, 2022.
- 911 Luo, L., Bai, X., Liu, S., Wu, B., Liu, W., Lv, Y., Guo, Z., Lin, S., Zhao, S., Hao, Y., Hao, J.,
912 Zhang, K., Zheng, A., and Tian, H.: Fine particulate matter (PM_{2.5}/PM_{1.0}) in Beijing,
913 China: variations and chemical compositions as well as sources, *J. Environ. Sci.*, 121,
914 187–198, <https://doi.org/10.1016/j.jes.2021.12.014>, 2022.
- 915 McClure, C. D., Lim, C. Y., Hagan, D. H., Kroll, J. H., and Cappa, C. D.: Biomass-burning-
916 derived particles from a wide variety of fuels - Part 1: Properties of primary particles,
917 *Atmos. Chem. Phys.*, 20, 1531–1547, <https://doi.org/10.5194/acp-20-1531-2020>, 2020.
- 918 Mylonaki, M., Gini, M., Georgopoulou, M., Pilou, M., Chalvatzaki, E., Solomos, S.,
919 Diapouli, E., Giannakaki, E., Lazaridis, M., Pandis, S. N., Nenes, A., Eleftheriadis, K.,
920 and Papayannis, A.: Wildfire and African dust aerosol oxidative potential, exposure and
921 dose in the human respiratory tract, *Sci. Total Environ.*, 913, 169683,
922 <https://doi.org/10.1016/j.scitotenv.2023.169683>, 2024.
- 923 Ng, N. L., Canagaratna, M. R., Zhang, Q., Jimenez, J. L., Tian, J., Ulbrich, I. M., Kroll, J. H.,
924 Docherty, K. S., Chhabra, P. S., Bahreini, R., Murphy, S. M., Seinfeld, J. H.,
925 Hildebrandt, L., Donahue, N. M., Decarlo, P. F., Lanz, V. A., Prévôt, A. S. H., Dinar, E.,
926 Rudich, Y., and Worsnop, D. R.: Organic aerosol components observed in Northern
927 Hemispheric datasets from aerosol mass spectrometry, *Atmos. Chem. Phys.*, 10, 4625–
928 4641, <https://doi.org/10.5194/acp-10-4625-2010>, 2010.
- 929 Ng, N. L., Tuet, W. Y., Chen, Y., Fok, S., Gao, D., Rodriguez, M. S. T., Klein, M., Grosberg,
930 A., Weber, R. J., and Champion, J. A.: Cellular and acellular assays for measuring
931 oxidative stress induced by ambient and laboratory-generated aerosols, *Res. Rep.*
932 *Health. Eff. Inst.*, 2019, 1–57, 2019.
- 933 Novakov, T., Menon, S., Kirchstetter, T. W., Koch, D., and Hansen, J. E.: Aerosol organic
934 carbon to black carbon ratios: analysis of published data and implications for climate
935 forcing, *J. Geophys. Res. Atmos.*, 110, 1–12, <https://doi.org/10.1029/2005jd005977>,
936 2005.
- 937 Nyström, R., Lindgren, R., Avagyan, R., Westerholm, R., Lundstedt, S., and Boman, C.:
938 Influence of wood species and burning conditions on particle emission characteristics in
939 a residential wood stove, *Energy & Fuels*, 31, 5514–5524,
940 <https://doi.org/10.1021/acs.energyfuels.6b02751>, 2017.



- 941 Othman, M., Latif, M. T., Hamid, H. H. A., Uning, R., Khumsaeng, T., Phairuang, W., Daud,
942 Z., Idris, J., Sofwan, N. M., and Lung, S. C. C.: Spatial–temporal variability and health
943 impact of particulate matter during a 2019–2020 biomass burning event in Southeast
944 Asia, *Sci. Rep.*, 12, 1–11, <https://doi.org/10.1038/s41598-022-11409-z>, 2022.
- 945 Paraskevopoulou, D., Bougiatioti, A., Stavroulas, I., Fang, T., Lianou, M., Liakakou, E.,
946 Gerasopoulos, E., Weber, R., Nenes, A., and Mihalopoulos, N.: Yearlong variability of
947 oxidative potential of particulate matter in an urban Mediterranean environment, *Atmos.*
948 *Environ.*, 206, 183–196, <https://doi.org/10.1016/j.atmosenv.2019.02.027>, 2019.
- 949 Paraskevopoulou, D., Bougiatioti, A., Zarnmpas, P., Tsagkaraki, M., Nenes, A., and
950 Mihalopoulos, N.: Impact of COVID-19 lockdown on oxidative potential of particulate
951 matter: case of Athens (Greece), *Toxics*, 10, 280,
952 <https://doi.org/10.3390/toxics10060280>, 2022.
- 953 Price-Allison, A., Mason, P. E., Jones, J. M., Barimah, E. K., Jose, G., Brown, A. E., Ross,
954 A. B., and Williams, A.: The impact of fuelwood moisture content on the emission of
955 gaseous and particulate pollutants from a wood stove, *Combust. Sci. Technol.*, 195,
956 133–152, <https://doi.org/10.1080/00102202.2021.1938559>, 2021.
- 957 Puthussery, J. V., Singh, A., Rai, P., Bhattu, D., Kumar, V., Vats, P., Furger, M., Rastogi, N.,
958 Slowik, J. G., Ganguly, D., Prevot, A. S. H., Tripathi, S. N., and Verma, V.: Real-time
959 measurements of PM_{2.5} oxidative potential using a dithiothreitol assay in Delhi, India,
960 *Environ. Sci. Technol. Lett.*, 7, 504–510, <https://doi.org/10.1021/acs.estlett.0c00342>,
961 2020.
- 962 Rao, L., Zhang, L., Wang, X., Xie, T., Zhou, S., Lu, S., Liu, X., Lu, H., Xiao, K., Wang, W.,
963 and Wang, Q.: Oxidative potential induced by ambient particulate matters with acellular
964 assays: a review, *Processes*, 8, 1–21, <https://doi.org/10.3390/pr8111410>, 2020.
- 965 Reid, W. V., Ali, M. K., Christopher, J., Field, B., Correspondence, W. V., Reid, D., and
966 Packard, L.: The future of bioenergy, *Glob. Chang. Biol.*, 26, 274–286,
967 <https://doi.org/10.1111/gcb.14883>, 2020.
- 968 Shen, G., Du, W., Luo, Z., Li, Y., Cai, G., Lu, C., Qiu, Y., Chen, Y., Cheng, H., and Tao, S.:
969 Fugitive emissions of CO and PM_{2.5} from indoor biomass burning in chimney stoves
970 based on a newly developed carbon balance approach, *Environ. Sci. Technol. Lett.*, 7,
971 128–134, <https://doi.org/10.1021/acs.estlett.0c00095>, 2020.
- 972 Srivastava, D., Vu, T. V., Tong, S., Shi, Z., and Harrison, R. M.: Formation of secondary
973 organic aerosols from anthropogenic precursors in laboratory studies, *Npj Clim. Atmos.*
974 *Sci.*, 5, 1–30, <https://doi.org/10.1038/s41612-022-00238-6>, 2022.
- 975 Stockwell, C. E., Yokelson, R. J., Kreidenweis, S. M., Robinson, A. L., Demott, P. J.,
976 Sullivan, R. C., Reardon, J., Ryan, K. C., Griffith, D. W. T., and Stevens, L.: Trace gas
977 emissions from combustion of peat, crop residue, domestic biofuels, grasses, and other
978 fuels: configuration and Fourier transform infrared (FTIR) component of the fourth Fire
979 Lab at Missoula Experiment (FLAME-4), *Atmos. Chem. Phys.*, 14, 9727–9754,
980 <https://doi.org/10.5194/acp-14-9727-2014>, 2014.
- 981 Sun, J., Wang, J., Shen, Z., Huang, Y., Zhang, Y., Niu, X., Cao, J., Zhang, Q., Xu, H., Zhang,
982 N., and Li, X.: Volatile organic compounds from residential solid fuel burning in
983 Guanzhong Plain, China: source-related profiles and risks, *Chemosphere*, 221, 184–192,
984 <https://doi.org/10.1016/j.chemosphere.2019.01.002>, 2019.



- 985 Sun, Y., Du, W., Fu, P., Wang, Q., Li, J., Ge, X., Zhang, Q., Zhu, C., Ren, L., Xu, W., Zhao,
986 J., Han, T., Worsnop, D. R., and Wang, Z.: Primary and secondary aerosols in Beijing in
987 winter: sources, variations and processes, *Atmos. Chem. Phys.*, 16, 8309–8329,
988 <https://doi.org/10.5194/acp-16-8309-2016>, 2016.
- 989 Tiitta, P., Leskinen, A., Hao, L., Yli-Pirilä, P., Kortelainen, M., Grigonyte, J., Tissari, J.,
990 Lamberg, H., Hartikainen, A., Kuusalo, K., Kortelainen, A. M., Virtanen, A., Lehtinen,
991 K. E. J., Komppula, M., Pieber, S., Prévôt, A. S. H., Onasch, T. B., Worsnop, D. R.,
992 Czech, H., Zimmermann, R., Jokiniemi, J., and Sippula, O.: Transformation of logwood
993 combustion emissions in a smog chamber: formation of secondary organic aerosol and
994 changes in the primary organic aerosol upon daytime and nighttime aging, *Atmos.*
995 *Chem. Phys.*, 16, 13251–13269, <https://doi.org/10.5194/acp-16-13251-2016>, 2016.
- 996 Tomlin, J. M., Weis, J., Veghte, D. P., China, S., Fraund, M., He, Q., Reicher, N., Li, C.,
997 Jankowski, K. A., Rivera-Adorno, F. A., Morales, A. C., Rudich, Y., Moffet, R. C.,
998 Gilles, M. K., and Laskin, A.: Chemical composition and morphological analysis of
999 atmospheric particles from an intensive bonfire burning festival, *Environ. Sci. Atmos.*,
1000 2, 616–633, <https://doi.org/10.1039/d2ea00037g>, 2022.
- 1001 Trubetskaya, A., Lin, C., Ovadnevaite, J., Ceburnis, D., O'Dowd, C., Leahy, J. J., Monaghan,
1002 R. F. D., Johnson, R., Layden, P., and Smith, W.: Study of emissions from domestic
1003 solid-fuel stove combustion in Ireland, *Energy & Fuels*, 35, 4966–4978,
1004 <https://doi.org/10.1021/acs.energyfuels.0c04148>, 2021.
- 1005 Tsiodra, I., Grivas, G., Tavernarakis, K., Bougiatioti, A., Apostolaki, M., Paraskevopoulou,
1006 D., Gogou, A., Parinos, C., Oikonomou, K., Tsagkaraki, M., Zampas, P., Nenes, A.,
1007 and Mihalopoulos, N.: Annual exposure to polycyclic aromatic hydrocarbons in urban
1008 environments linked to wintertime wood-burning episodes, *Atmos. Chem. Phys.*, 21,
1009 17865–17883, <https://doi.org/10.5194/acp-21-17865-2021>, 2021.
- 1010 Tsiodra, I., Grivas, G., Bougiatioti, A., Tavernarakis, K., Parinos, C., Paraskevopoulou, D.,
1011 Papoutsidaki, K., Tsagkaraki, M., Kozonaki, F. A., Oikonomou, K., Nenes, A., and
1012 Mihalopoulos, N.: Source apportionment of particle-bound polycyclic aromatic
1013 hydrocarbons (PAHs), oxygenated PAHs (OPAHs), and their associated long-term
1014 health risks in a major European city, *Sci. Total Environ.*, 951,
1015 <https://doi.org/10.1016/j.scitotenv.2024.175416>, 2024.
- 1016 Tuet, W. Y., Chen, Y., Xu, L., Fok, S., Gao, D., Weber, R. J., and Ng, N. L.: Chemical
1017 oxidative potential of secondary organic aerosol (SOA) generated from the
1018 photooxidation of biogenic and anthropogenic volatile organic compounds, *Atmos*
1019 *Chem Phys*, 17, 839–853, <https://doi.org/10.5194/ACP-17-839-2017>, 2017.
- 1020 Vasilakopoulou, C. N., Matrali, A., Skyllakou, K., Georgopoulou, M., Aktypis, A., Florou,
1021 K., Kaltsonoudis, C., Siouti, E., Kostenidou, E., Błaziak, A., Nenes, A., Papagiannis, S.,
1022 Eleftheriadis, K., Patoulas, D., Kioutsoukis, I., and Pandis, S. N.: Rapid transformation
1023 of wildfire emissions to harmful background aerosol, *Npj Clim. Atmos. Sci.*, 6, 1–9,
1024 <https://doi.org/10.1038/s41612-023-00544-7>, 2023.
- 1025 Verma, V., Fang, T., Xu, L., Peltier, R. E., Russell, A. G., Ng, N. L., and Weber, R. J.:
1026 Organic aerosols associated with the generation of reactive oxygen species (ROS) by
1027 water-soluble PM_{2.5}, *Environ. Sci. Technol.*, 49, 4646–4656,
1028 <https://doi.org/10.1021/es505577W>, 2015.



- 1029 Wang, N., Jorga, S. D., Pierce, J. R., Donahue, N. M., and Pandis, S. N.: Particle wall-loss
1030 correction methods in smog chamber experiments, *Atmos. Meas. Tech.*, 11, 6577–6588,
1031 <https://doi.org/10.5194/amt-11-6577-2018>, 2018.
- 1032 Wang, S., Gallimore, P. J., Liu-Kang, C., Yeung, K., Campbell, S. J., Uttinger, B., Liu, T.,
1033 Peng, H., Kalberer, M., Chan, A. W. H., and Abbatt, J. P. D.: Dynamic wood smoke
1034 aerosol toxicity during oxidative atmospheric aging, *Environ. Sci. Technol.*, 57, 1246–
1035 1256, <https://doi.org/10.1021/acs.est.2c05929>, 2023.
- 1036 Wong, J. P. S., Tsagkaraki, M., Tsiodra, I., Mihalopoulos, N., Violaki, K., Kanakidou, M.,
1037 Sciare, J., Nenes, A., and Weber, R. J.: Effects of atmospheric processing on the
1038 oxidative potential of biomass burning organic aerosols, *Environ. Sci. Technol.*, 53,
1039 6747–6756, <https://doi.org/10.1021/acs.est.9b01034>, 2019.
- 1040 Yazdani, A., Takahama, S., Kodros, J. K., Paglione, M., Paglione, M., Masiol, M., Squizzato,
1041 S., Florou, K., Kaltsonoudis, C., Jorga, S. D., Pandis, S. N., Pandis, S. N., Nenes, A.,
1042 and Nenes, A.: Chemical evolution of primary and secondary biomass burning aerosols
1043 during daytime and nighttime, *Atmos. Chem. Phys.*, 23, 7461–7477,
1044 <https://doi.org/10.5194/acp-23-7461-2023>, 2023.
- 1045 Yokelson, R. J., Griffith, D. W. T., and Ward, D. E.: Open-path Fourier transform infrared
1046 studies of large-scale laboratory biomass fires, *J. Geophys. Res. Atmos.*, 101, 21067–
1047 21080, <https://doi.org/10.1029/96jd01800>, 1996.
- 1048 Zauli-Sajani, S., Thunis, P., Pisoni, E., Bessagnet, B., Monforti-Ferrario, F., De Meij, A.,
1049 Pekar, F., and Vignati, E.: Reducing biomass burning is key to decrease PM_{2.5} exposure
1050 in European cities, *Sci. Rep.*, 14, 1–11, <https://doi.org/10.1038/s41598-024-60946-2>,
1051 2024.
- 1052 Zhang, Y., Kong, S., Sheng, J., Zhao, D., Ding, D., Yao, L., Zheng, H., Wu, J., Cheng, Y.,
1053 Yan, Q., Niu, Z., Zheng, S., Wu, F., Yan, Y., Liu, D., and Qi, S.: Real-time emission and
1054 stage-dependent emission factors/ratios of specific volatile organic compounds from
1055 residential biomass combustion in China, *Atmos. Res.*, 248, 105189,
1056 <https://doi.org/10.1016/j.atmosres.2020.105189>, 2021.
- 1057 Zhang, Z. H., Hartner, E., Uttinger, B., Gfeller, B., Paul, A., Sklorz, M., Czech, H., Yang, B.
1058 X., Su, X. Y., Jakobi, G., Orasche, J., Schnelle-Kreis, J., Jeong, S., Gröger, T., Pardo,
1059 M., Hohaus, T., Adam, T., Kiendler-Scharr, A., Rudich, Y., Zimmermann, R., and
1060 Kalberer, M.: Are reactive oxygen species (ROS) a suitable metric to predict toxicity of
1061 carbonaceous aerosol particles?, *Atmos. Chem. Phys.*, 22, 1793–1809,
1062 <https://doi.org/10.5194/acp-22-1793-2022>, 2022.
- 1063



Table 1: Initial biomass burning aerosol composition and initial chamber conditions for all the conducted experiments.

Exp.	PM ₁ [μg m ⁻³]	BC [μg m ⁻³]	Amm oniun [μg m ⁻³]	Sulfat e [μg m ⁻³]	Orga nics [μg m ⁻³]	Nitrat e [μg m ⁻³]	Org. Nitrat e [μg m ⁻³]	Inorg. Nitrat e [μg m ⁻³]	Chlor ide [μg m ⁻³]	f_{44}/f_{60}	O:C	H:C	RH _{init} [%]	MCE*
DN1	70	3.7	0.06	0.62	63.6	1.18	0.56	0.62	0.45	1.37	0.43	1.67	13	0.96
DN2	114	7.9	0.13	0.86	102	2.01	1	1.01	0.42	2.21	0.39	1.66	N/A	0.92
DN3	79.1	N/A	8.1	22.1	48.2	0.52	0.23	0.29	0.11	1.82	0.38	1.62	N/A	0.99
DN4	177	1.1	0.24	1.11	172	2.02	0.91	1.11	0.62	1.11	0.39	1.71	N/A	0.91
DN5	102	0.4	0.09	0.47	99.8	0.65	0.26	0.39	0.19	1.00	0.35	1.72	N/A	0.99
DN6	53.6	0.9	0.07	1.02	49.6	1.66	1.02	0.64	0.41	1.50	0.36	1.76	N/A	0.96
DN7	74.8	0.8	0.06	0.54	72.1	1.15	0.43	0.72	0.16	1.34	0.41	1.67	N/A	0.91
DN8	85.5	5.4	0.09	0.49	78.0	1.22	0.28	0.94	0.33	1.02	0.44	1.65	13	0.92
ND1	121	N/A	0.28	1.01	118	1.21	0.66	0.55	0.58	1.72	0.41	1.65	13	0.92
ND2	72.0	0.5	0.21	0.45	69.4	1.13	0.76	0.37	0.24	2.53	0.47	1.67	N/A	0.96
ND3	47.2	0.4	0.16	0.12	45.8	0.67	0.34	0.33	0.05	2.37	0.29	1.67	14	0.94
ND4	93.3	1	0.22	0.54	90.2	0.99	0.50	0.49	0.34	1.61	0.40	1.66	15	0.92
ND5	176	N/A	0.25	0.34	174	1.35	0.62	0.73	0.18	1.27	0.37	1.66	13	0.91
ND6	124	3	0.18	0.41	120	0.72	0.31	0.41	0.38	0.92	0.43	1.65	14	0.90
ND7	126	67	0.06	0.07	58.7	0.15	0.10	0.05	0.05	2.47	0.23	1.61	12	0.98
ND8	276	190	0.12	0.62	83.4	1.22	0.85	0.37	0.25	1.88	0.36	1.65	24	0.96

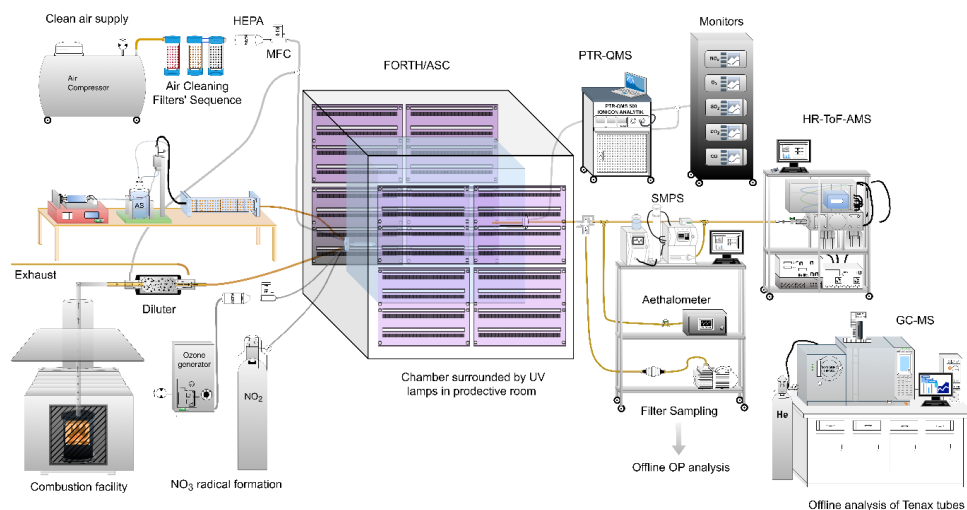
*Modified combustion efficiency (MCE) calculated based on equation: $([\Delta\text{CO}_2]/([\Delta\text{CO}]+[\Delta\text{CO}_2]))$.



Table 2: Composition of aged biomass burning aerosol, averaged over the last 30 minutes of each oxidation state, for both daytime-first (DN) and nighttime-first (ND) experiments.

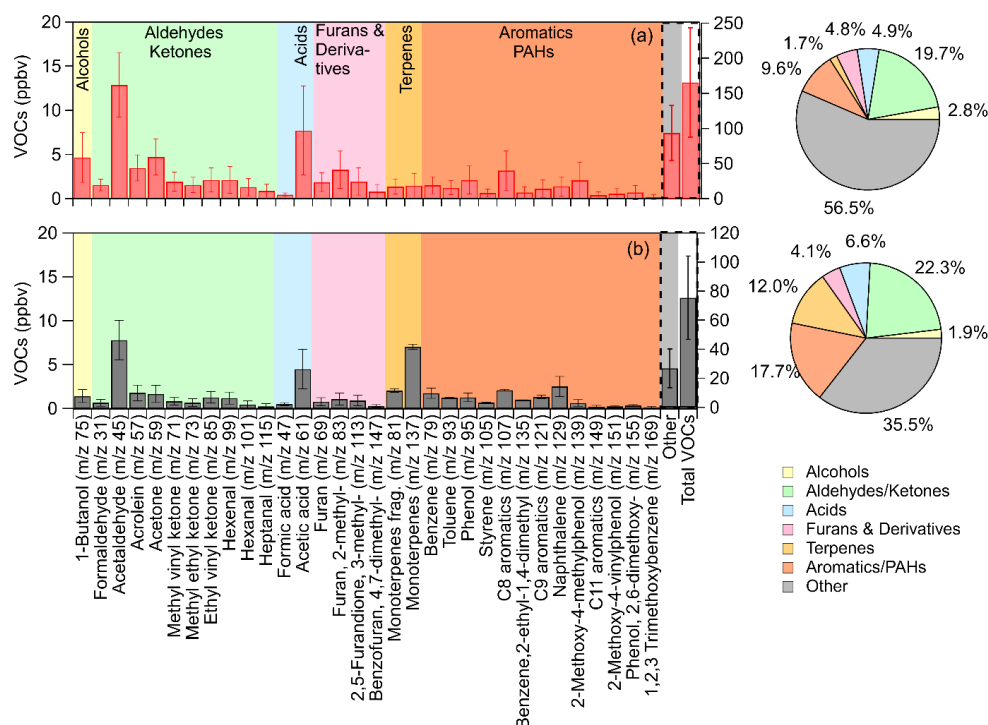
Exp.	Oxid.	PM ₁ [μg m ⁻³]	Amm oniu n [μg m ⁻³]	Sulfate [μg m ⁻³]	Organi cs [μg m ⁻³]	Nitrate [μg m ⁻³]	Org. Nitrate [μg m ⁻³]	Inorg. Nitrate [μg m ⁻³]	Chlor ide [μg m ⁻³]	ρ* [g cm ⁻³]	<i>f₄₄/f₆₀</i>	O:C	H:C
Day - Night													
DN1	Day	88	0.1	0.7	85	1.76	0.86	0.90	0.38	1.34	4.3	0.58	1.61
	Night	104	0.15	0.83	100	2.74	1.48	1.26	0.4		5.1	0.61	1.6
DN2	Day	157	0.1	0.9	154	2.42	1.75	0.67	0.26	1.34	15.3	0.64	1.52
	Night	185	0.47	1.46	179	4.21	2.98	1.23	0.3		16.5	0.67	1.53
DN3	Day	102	10.3	28.9	62	0.63	0.36	0.27	0.13	1.37	8.5	0.63	1.55
	Night	107	10.8	30.3	65	0.94	0.61	0.33	0.15		9.7	0.64	1.55
DN4	Day	240	1.1	1.2	232	4.92	2.29	2.63	0.49	1.32	3.7	0.58	1.64
	Night	262	1.26	1.35	252	6.14	2.82	3.32	0.52		3.9	0.6	1.64
DN5	Day	134	0.1	0.5	132	0.97	0.52	0.45	0.18	1.29	3.4	0.52	1.66
	Night	156	0.19	0.59	153	2.19	1.51	0.68	0.2		4.3	0.56	1.65
DN6	Day	83	0.2	1.3	78	2.80	1.55	1.25	0.38	1.33	6.5	0.59	1.63
	Night	90	0.22	1.48	85	3.27	1.78	1.49	0.4		7.1	0.61	1.61
DN7	Day	105	0.1	0.6	103	1.43	0.69	0.74	0.15	1.34	5.4	0.6	1.61
	Night	122	0.17	0.79	119	1.94	1.03	0.91	0.17		5.8	0.62	1.61
DN8	Day	111	0.1	0.6	108	1.68	0.59	1.09	0.33	1.33	3	0.58	1.61
	Night	134	0.19	0.74	130	2.95	1.37	1.58	0.36		3.4	0.6	1.6
Night – Day													
ND1	Night	199	1.2	1.1	188	9.0	5.4	3.6	0.28	1.36	5.5	0.55	1.61
	Day	233	1.5	1.3	222	8.7	5.0	3.7	0.29		9	0.66	1.58
ND2	Night	110	0.5	0.5	102	7.0	5.5	1.5	0.15	1.39	8.1	0.62	1.6
	Day	119	0.6	0.6	112	6.3	4.8	1.5	0.16		11.1	0.7	1.57
ND3	Night	61	0.2	0.2	57	2.9	2.2	0.7	0.06	1.28	7.3	0.42	1.64
	Day	66	0.3	0.2	63	2.5	1.9	0.6	0.07		12.2	0.52	1.61
ND4	Night	133	0.4	0.8	127	4.3	3.1	1.2	0.29	1.31	3.9	0.49	1.62
	Day	148	0.6	1	142	4.2	2.9	1.3	0.3		6.4	0.58	1.6
ND5	Night	278	0.5	0.5	270	7.0	4.8	2.2	0.14	1.31	3.8	0.48	1.63
	Day	315	0.7	0.6	307	6.6	4.0	2.6	0.14		6.5	0.58	1.61
ND6	Night	192	0.7	0.6	184	6.8	4.1	2.7	0.18	1.33	2.6	0.51	1.62
	Day	203	0.8	0.7	195	6.0	3.4	2.6	0.19		4.8	0.61	1.61
ND7	Night	182	0.1	0.1	93	4.6	3.1	1.5	0.06	1.2	5	0.36	1.65
	Day	211	0.1	0.2	105	4.7	3.0	1.7	0.08		6.5	0.41	1.62
ND8	Night	400	0.3	1.2	149	9.3	5.4	3.9	0.26	1.29	4.7	0.48	1.64
	Day	451	0.5	1.7	163	9.1	5.2	3.9	0.29		7.6	0.54	1.6

*Density calculated based on O:C and H:C ratios, following the approach of Kuwata et al. (2012).



1070

1071 **Figure 1:** Experimental setup of the FORTH-ASC facility, illustrating the surrounding
1072 instrumentation and the combustion facility.

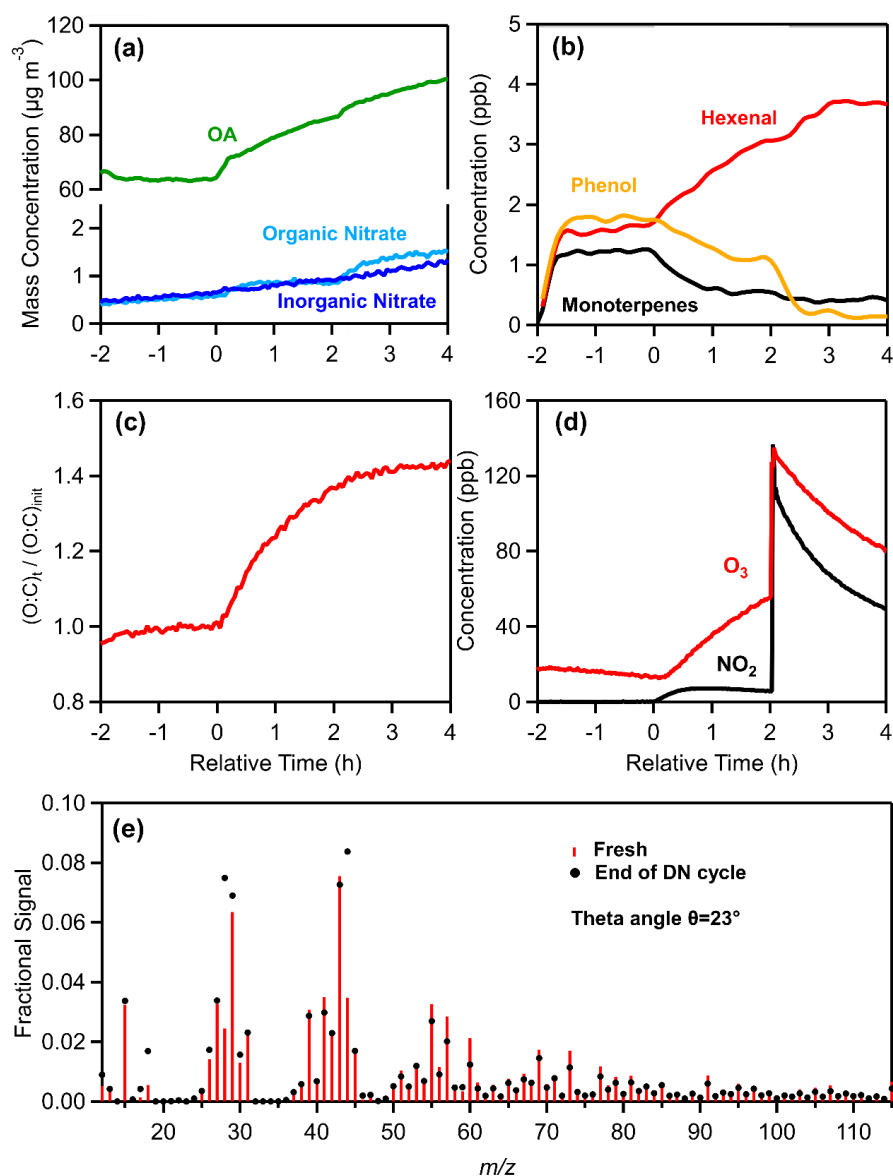


1073

1074 **Figure 2:** Average concentrations, in ppbv, of the identified VOCs in (a) fresh olive wood
 1075 burning emissions (red bars) and (b) fresh olive-pine mixed emissions (grey bars), along with
 1076 their percentage contribution to the total VOCs concentration measured by PTR-QMS. The
 1077 protonated m/z for each compound is shown in parentheses on the x-axis. The left y-axis shows
 1078 the concentrations of identified VOCs, while the right y-axis displays the concentrations of the
 1079 sum of the unidentified (other) and the total measured VOCs.



1080

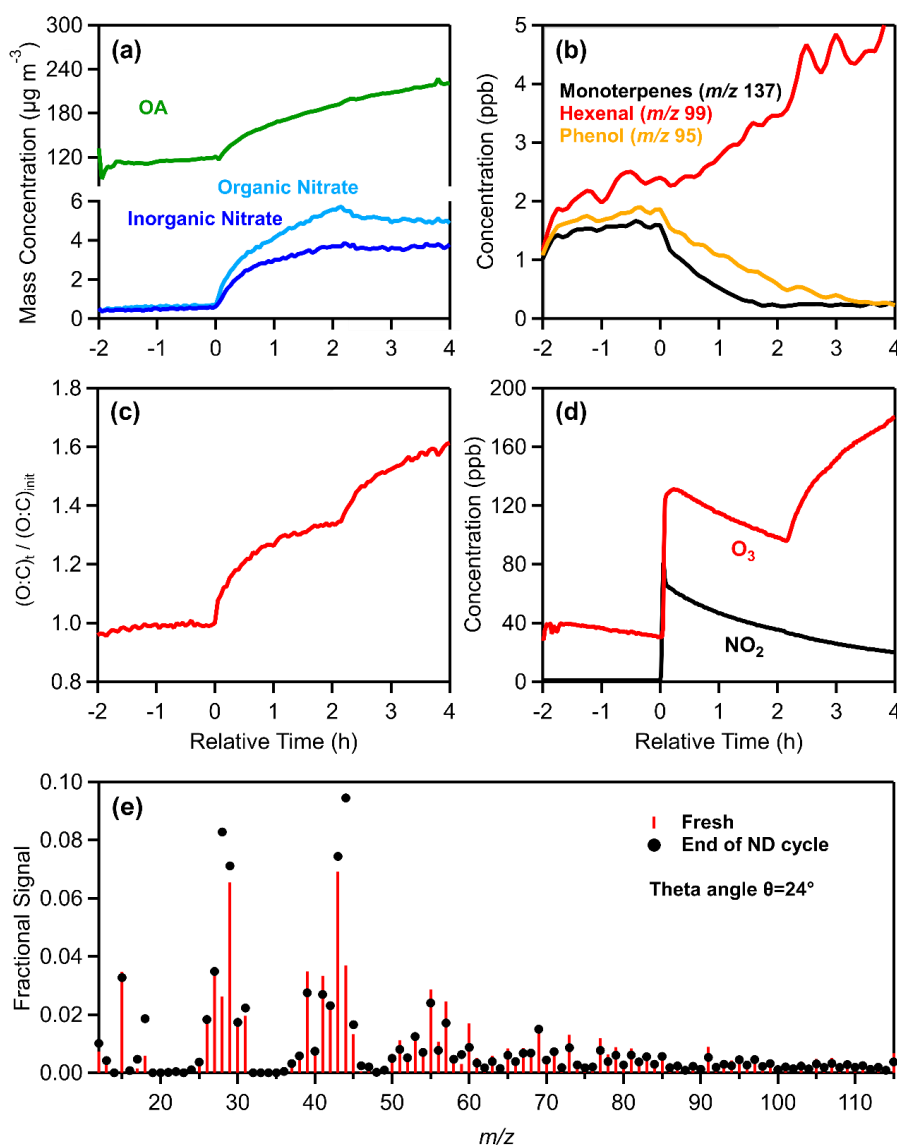


1081

1082 **Figure 3:** Measurements from the experiment DN1, showing the time evolution of: (a) wall-
1083 loss-corrected organic aerosol, particulate organic and inorganic nitrate, (b) selected VOCs,
1084 including monoterpenes (m/z 137), hexenal (m/z 99), and phenol (m/z 95), (c) normalized O:C
1085 ratio, (d) O_3 and NO_2 , and (e) a comparison of the fresh (red sticks) and nighttime (black
1086 markers) oxidized aerosol mass spectra at the end of the daytime-first oxidation cycle.



1087

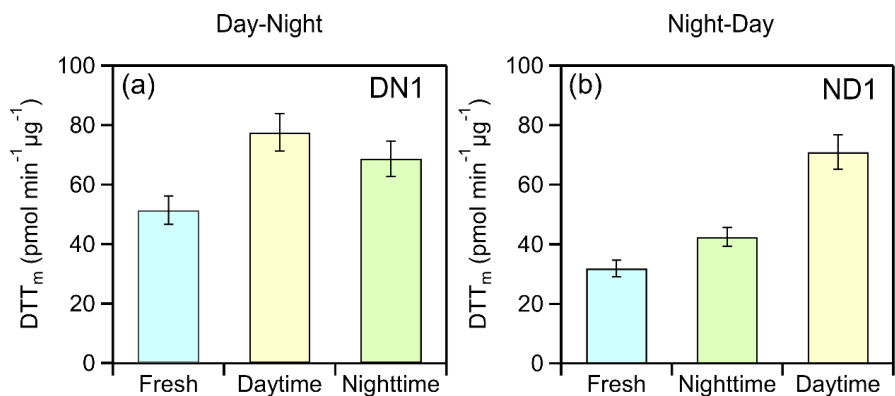


1088

Figure 4: Measurements from the experiment ND1, showing the time evolution of: (a) wall-loss-corrected organic aerosol, particulate organic and inorganic nitrate, (b) selected VOCs, including monoterpenes (m/z 137), hexenal (m/z 99), and phenol (m/z 95), (c) normalized O:C ratio, (d) O_3 and NO_2 , and (e) a comparison of the fresh (red sticks) and daytime (black markers) oxidized aerosol mass spectra at the end of the nighttime-first oxidation cycle.



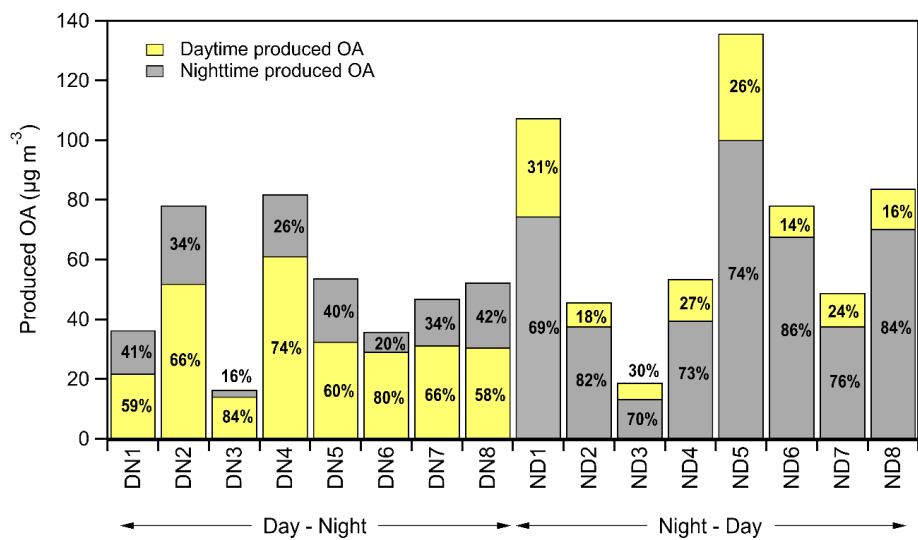
1094



1095

1096 **Figure 5:** Category plots illustrating the evolution in water-soluble oxidative potential (WS-
1097 OP), expressed as per OC mass normalized DTT_m activity (pmol min⁻¹ µg⁻¹), in case of typical
1098 experiment (a) DN1 and (b) ND1.

1099

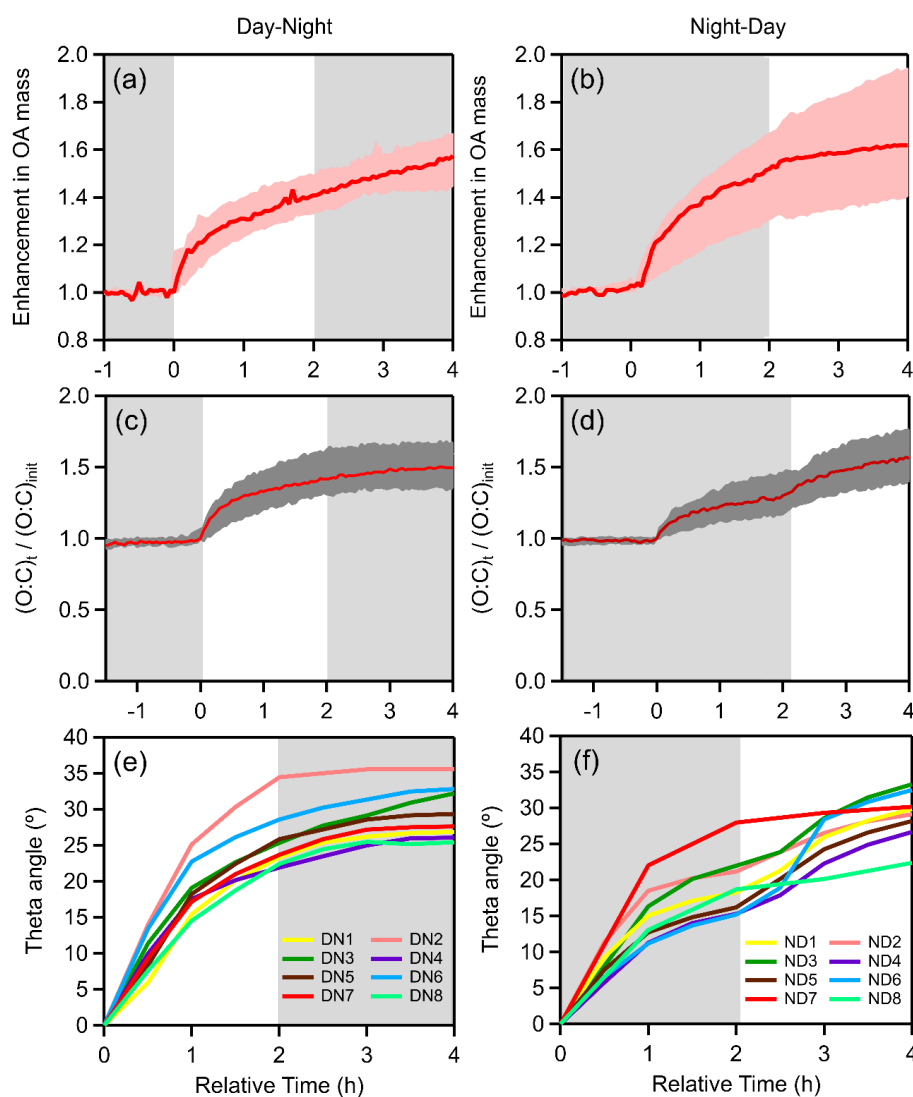


1100

1101 **Figure 6:** Absolute mass (in µg m⁻³) and percentage increase (%) of OA (including organic
1102 nitrate) per oxidation regime (daytime, nighttime) for both daytime-first (DN) and nighttime-
1103 first (ND) cycles, for all conducted experiments.



1104

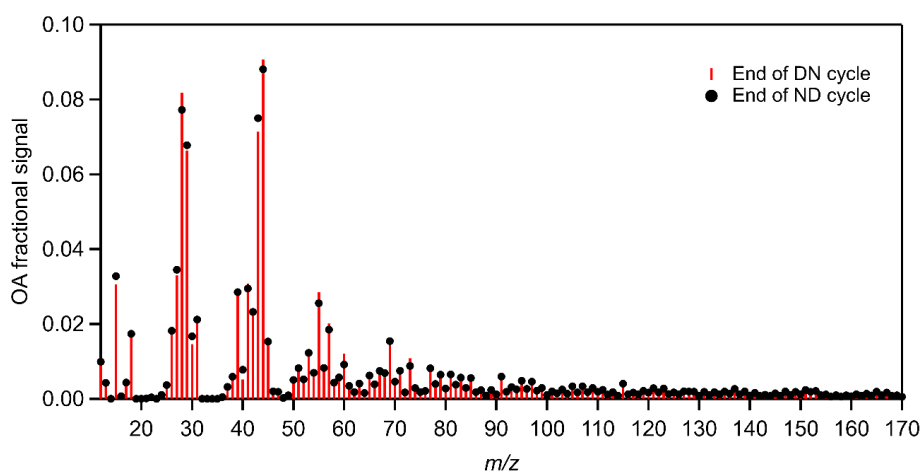


1105

Figure 7: Evolution over time of: OA enhancement during (a) daytime-first and (b) nighttime-first oxidation cycle; O:C ratio enhancement during (c) daytime-first and (d) nighttime-first oxidation cycle; theta angle during (e) daytime-first and (f) nighttime-first oxidation for experiments conducted under dry initial conditions using only olive wood logs as burning fuel (DN1-DN8, ND1-ND6). In experiments ND3, ND4, and ND6, the change in spectrum occurred slightly later, as the first-step oxidation extended to 3 h compared to 2 h lasted in the other nighttime-first experiments.



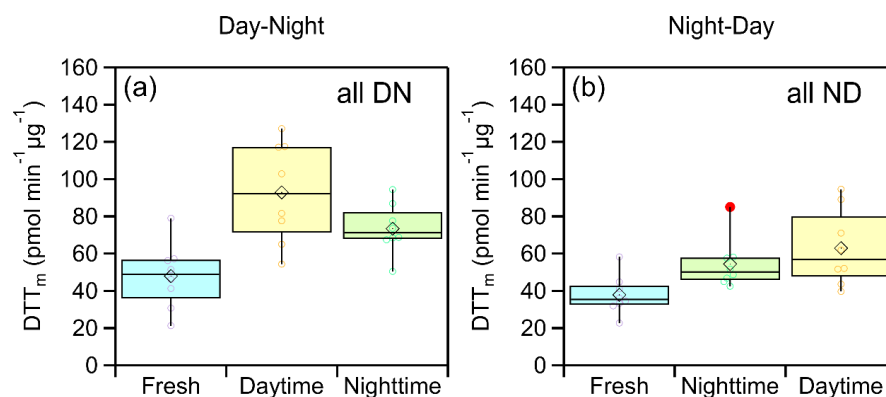
1113



1114

1115 **Figure 8:** Relative differences in the average spectra obtained at the end of daytime-first (DN,
1116 red sticks) and nighttime-first (ND, black circles) oxidation cycle, respectively, for experiments
1117 conducted using olive wood logs as burning fuel. The theta angle between the averaged aged
1118 daytime- and nighttime-first aged spectra was 3° (identical).

1119



1120

1121 **Figure 9:** Box plots illustrating the changes in WS-OP, expressed as per OC mass normalized
1122 DTT_m activity ($\text{pmol min}^{-1} \mu\text{g}^{-1}$), considering all performed experiments, in case of (a) daytime
1123 first (DN) oxidation cycle and (b) nighttime-first (ND) oxidation cycle.